

Electron transport in quantum channels with spin–orbit interaction: effects of the sign of the Rashba coupling and applications to nanowires

*Original*

Electron transport in quantum channels with spin–orbit interaction: effects of the sign of the Rashba coupling and applications to nanowires / Gogin, L., Rossi, F., Dolcini, F.. - In: NEW JOURNAL OF PHYSICS. - ISSN 1367-2630. - STAMPA. - 24:9(2022), p. 093025. [10.1088/1367-2630/ac8f66]

*Availability:*

This version is available at: 11583/2972026 since: 2022-10-04T05:42:38Z

*Publisher:*

IOP Publishing Ltd

*Published*

DOI:10.1088/1367-2630/ac8f66

*Terms of use:*

This article is made available under terms and conditions as specified in the corresponding bibliographic description in the repository

*Publisher copyright*

(Article begins on next page)

PAPER • OPEN ACCESS

## Electron transport in quantum channels with spin–orbit interaction: effects of the sign of the Rashba coupling and applications to nanowires

To cite this article: Leonid Gogin *et al* 2022 *New J. Phys.* **24** 093025

View the [article online](#) for updates and enhancements.

### You may also like

- [Rashba coupling and spin switching through surface states of Dirac semimetals](#)  
Yuriko Baba, Francisco Domínguez-Adame, Gloria Platero *et al.*
- [Identifying the graphene \*d\*-wave superconducting symmetry by an anomalous splitting zero-bias conductance peak](#)  
Chuan-Shuai Huang, Yang Yang, Y C Tao *et al.*
- [The influence of the Rashba spin–orbit coupling on the two-dimensional magnetoexcitons](#)  
T Hakiolu, M A Liberman, S A Moskalenko *et al.*



## PAPER

# Electron transport in quantum channels with spin-orbit interaction: effects of the sign of the Rashba coupling and applications to nanowires

## OPEN ACCESS

RECEIVED  
8 July 2022REVISED  
25 August 2022ACCEPTED FOR PUBLICATION  
5 September 2022PUBLISHED  
19 September 2022

Original content from  
this work may be used  
under the terms of the  
[Creative Commons  
Attribution 4.0 licence](#).

Any further distribution  
of this work must  
maintain attribution to  
the author(s) and the  
title of the work, journal  
citation and DOI.



Leonid Gogin , Fausto Rossi and Fabrizio Dolcini\*

Dipartimento di Scienza Applicata e Tecnologia del Politecnico di Torino, I-10129 Torino, Italy

\* Author to whom any correspondence should be addressed.

E-mail: [fabrizio.dolcini@polito.it](mailto:fabrizio.dolcini@polito.it)**Keywords:** spin-orbit interaction, quantum transport, nanowires, scattering matrix formalism

## Abstract

We investigate the effects of the sign of the Rashba spin-orbit coupling (RSOC) on electron transmission through a single-channel nanowire (NW) in the quantum coherent regime. We show that, while for a finite length NW with homogeneous RSOC contacted to two electrodes the sign of its RSOC does not affect electron transport, the situation can be quite different in the presence of an inhomogeneous RSOC and a magnetic field applied along the NW axis. By analyzing transport across an interface between two regions of different RSOC we find that, if the two regions have equal RSOC signs, the transmission within the magnetic gap energy range is almost perfect, regardless of the ratio of the spin-orbit energies to the Zeeman energy. In contrast, when the two regions have opposite RSOC signs and are Rashba-dominated, the transmission gets suppressed. Furthermore, we discuss the implementation on a realistic NW setup where two RSOC regions are realized with suitably coupled gates separated by a finite distance. We find that the low-temperature NW conductance exhibits a crossover from a short distance behavior that strongly depends on the relative RSOC sign of the two regions to a large distance oscillatory behavior that is independent of such relative sign. We are thus able to identify the conditions where the NW conductance mainly depends on the sign of the RSOC and the ones where only the RSOC magnitude matters.

## 1. Introduction

Over the last 10 years most of research on semiconductor nanowires (NWs) with Rashba spin-orbit coupling (RSOC) has focussed on the search for Majorana quasi-particles, which are believed to provide the building block for topologically protected quantum information [1–6]. Although signatures compatible with these exotic quasi-particles have been found in NWs proximized by superconducting films [7–14], the race to the evidence of Majorana states has somewhat overshadowed other interesting potentialities of NWs in quantum technologies.

Indeed NWs reaching lengths of various  $\mu\text{m}$  and exhibiting quantum coherent transport are nowadays fabricated both in the clean ballistic [14–24] and in the diffusive regime [25], and are also realized in suspended geometries [9, 26], in arrays [24, 27, 28] and in networks [23]. Moreover, they can be used as flexible substrates for hybrid epitaxial growth on selected facets in order to design heterostructures with ferromagnets and superconductors [29]. Also, NWs represent an extremely versatile and tunable platform for nanoelectronics since their conduction properties can be controlled both magnetically, e.g. by applying a magnetic field along the NW axis and thereby opening up a gap in the spectrum, or electrically by controlling the RSOC through gate voltages. In particular, the tremendous improvement in gating techniques enables one to achieve a high control of the RSOC [30–35].

Most of these efforts have been devoted to enhance the *magnitude* of the RSOC over a wide range of values [36–46]. However, when an electron travels through a given spin-orbit region, its spin polarization

depends not only on the magnitude, but also on the *sign* of the local spin–orbit coupling. Are there any observable effects that can be attributed to the sign? So far, this question has been addressed only in a few cases. Concerning the Dresselhaus spin–orbit coupling, its sign reversal has been investigated in InGaAs rings [47], whereas in the case of the RSOC the problem has mainly been addressed in two-dimensional quantum wells interfaced with other suitable materials [48–50] or where bulk subbands are characterized by opposite RSOC signs [51]. As far as one-dimensional single-channel NWs are concerned, it has been shown that a spatially modulated RSOC with alternating sign can drive the transition from a metallic to an insulating state [52]. Moreover, when a NW is exposed to a magnetic field along its axis and the RSOC magnitude is large, the propagating states in the magnetic gap exhibit a locking between propagation direction and spin, whose helicity is determined by the RSOC sign [53–57]. Nevertheless, when the NW with homogeneous RSOC is contacted to two electrodes, the electron transport turns out to depend only on the magnitude of the RSOC, and not on its sign, as we shall see below. Recent studies suggest that a different scenario may emerge in the presence of inhomogeneous RSOC profile. A junction between two regions with opposite RSOC signs, for instance, exhibits interesting spectral and equilibrium properties at the interface, such as localized bound states [58, 59] and orthogonal spin polarization [60], which look surprisingly similar to the ones of the topological phase. In experimental implementations, where the RSOC can be locally controlled by gates, these inhomogeneous configurations can be realized by coupling various gates along the NW, providing an additional knob to control the electrical current flowing through the NW setup.

The question arises whether in such inhomogeneous configurations the sign of the RSOC can lead to any observable effect on out of equilibrium properties. In this paper we investigate this problem by analyzing the electron transport through a single-channel NW with inhomogeneous RSOC in the coherent quantum limit. The paper is organized as follows. In section 2 we present the model and describe the adopted method. Then, in section 3 we discuss the two necessary ingredients to observe the effects of the sign of the RSOC, namely the presence of a uniform magnetic field and the existence of at least two regions with different RSOC. In section 4 we first perform a preliminary analysis of the transmission in the presence of a single interface separating two regions with different RSOC, finding a quite different behavior of the electrical conductance in the cases of equal and opposite RSOC signs. Then, by analyzing a more realistic configuration, where two differently gated portions of a NW are separated by a finite distance, we show that such lengthscale can modify the results obtained in the ideal limit of one single interface case. This enables us to identify the conditions where the sign of the RSOC affects the NW transport properties, and the situations where only the RSOC magnitude matters. Finally, in section 6 we discuss our results and draw our conclusions.

## 2. Model and method

We consider a one-dimensional electron conduction channel directed along the  $x$  direction, characterized by a spatially varying RSOC profile and exposed to an external Zeeman magnetic field directed along its axis. The second-quantized Hamiltonian reads

$$\hat{H} = \int \hat{\Psi}^\dagger(x) \left( \frac{p_x^2}{2m^*} \sigma_0 - \frac{\sigma_z}{2\hbar} \{ \alpha(x), p_x \} - \sigma_x h_\perp \right) \hat{\Psi}(x), \quad (1)$$

where  $m^*$  denotes the effective electron mass. In order to ensure Hermiticity, a half of the anticommutator between the momentum operator  $p_x$  and the spatially inhomogeneous RSOC  $\alpha(x)$  has been introduced, as customary [61–64]. Here  $\sigma_x, \sigma_y, \sigma_z$  denote spin Pauli matrices, while  $\sigma_0$  is the  $2 \times 2$  identity. Moreover,  $z$  is the direction of the RSOC effective magnetic field, whereas  $x$  is the direction of the actual magnetic field, characterized by an energy coupling  $h_\perp = eg\hbar B/4m_e$ , where  $e$  denotes the electron charge,  $g$  the  $g$ -factor and  $m_e$  the bare electron mass.

We are interested in describing electron transport along the inhomogeneous channel. With respect to spin degenerate problems, the charge current operator exhibits an additional term related to the RSOC [65, 66]

$$\hat{j}^c(x, t) = -\frac{ie\hbar}{2m^*} \left( \hat{\Psi}^\dagger(x, t) \partial_x \hat{\Psi}(x, t) - \partial_x \hat{\Psi}^\dagger(x, t) \hat{\Psi}(x, t) \right) - \frac{e\alpha(x)}{\hbar} \hat{\Psi}^\dagger \sigma_z \hat{\Psi}, \quad (2)$$

as can be deduced from the very continuity equation  $\partial_t \hat{n} + \partial_x \hat{j}^c = 0$  following from the Heisenberg equation dictated by the Hamiltonian (1), where the charge density is  $\hat{n} = e\hat{\Psi}^\dagger \hat{\Psi}$ .

## 2.1. Relation with a magnetic texture problem

Before discussing any specific RSOC profile, we note a general property of the Hamiltonian (1). By performing the transformation [61, 67]

$$\hat{\Psi}(x) = e^{i\phi_{\text{SO}}(x)\frac{\sigma_z}{2}} \hat{\Psi}'(x) \quad (3)$$

where

$$\phi_{\text{SO}}(x) = \frac{2m^*}{\hbar^2} \int_{x_0}^x \alpha(x') dx' \quad (4)$$

and  $x_0$  is an arbitrarily fixed reference point, the Hamiltonian (1) is rewritten in the new fields  $\hat{\Psi}'(x)$  as

$$\hat{\mathcal{H}} = \int \hat{\Psi}'^\dagger(x) \left( \frac{p_x^2}{2m^*} + U_{\text{SO}}(x) - h_\perp (\cos[\phi_{\text{SO}}(x)]\sigma_x + \sin[\phi_{\text{SO}}(x)]\sigma_y) \right) \hat{\Psi}'(x) dx \quad (5)$$

where

$$U_{\text{SO}}(x) = -\frac{m^* \alpha^2(x)}{2\hbar^2}. \quad (6)$$

Various aspects are noteworthy. First, in the absence of Zeeman field ( $h_\perp = 0$ ), while for a homogeneous problem equation (6) is just a mere energy constant and the spin-orbit coupling gets completely gauged out, in an inhomogeneous problem the spatial profile of the effective scalar potential  $U_{\text{SO}}(x)$  does affect electron transmission, although in a spin-independent way [68]. For instance, in the case of a piecewise constant RSOC,  $U_{\text{SO}}(x)$  acquires the form of a potential step, a quantum well or a barrier, leading to an energy dependent transmission. The second aspect is that, when the Zeeman term  $h_\perp$  is additionally present, the last term of equation (5) acquires the form of a magnetic texture in the spin  $x$ - $y$  plane characterized by the rotation angle  $\phi_{\text{SO}}(x)$  in equation (4), which represents the integrated local spin-orbit wavevector (multiplied by 2). In this case the role of the spin degree of freedom becomes not trivial because of the interplay between actual magnetic field and spin-orbit effective magnetic field. In the following, we shall occasionally refer to the mapping to equation (5) in order to interpret some of our results.

## 2.2. Piecewise constant profile

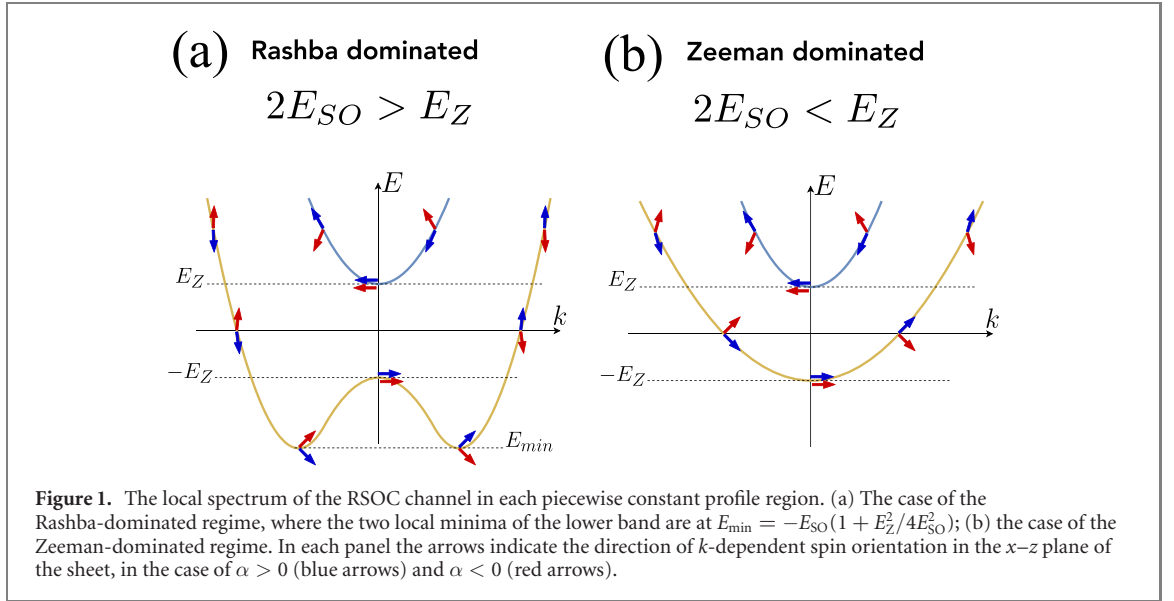
Although for an arbitrary spatial profile the inhomogeneous problem cannot be solved analytically, any profile  $\alpha(x)$  can ultimately be approximated with a piecewise constant profile, where the solution can be build up by suitably matching the electron field operator in each region. It is thus worth recalling briefly the main physical ingredients characterizing each locally homogeneous region. In a region with RSOC  $\alpha_j$  one identifies two energy scales, namely the spin-orbit energy

$$E_{\text{SO},j} = \frac{m^* \alpha_j^2}{2\hbar^2} \quad (7)$$

and the Zeeman energy

$$E_Z = |h_\perp| \quad (8)$$

which directly impact on the local spectrum. Indeed it consists of two bands (see figure 1), separated by a gap  $\Delta = 2E_Z$  at  $k = 0$ , where the lower band exhibits one minimum or two minima depending on whether the region is in the Zeeman-dominated regime ( $2E_{\text{SO},j} < E_Z$ ) or in the Rashba-dominated regime ( $2E_{\text{SO},j} > E_Z$ ). The classification of the eigenstates is in principle straightforward, although it requires a little more care in practice. First, while the spectrum does not depend on the sign of the RSOC  $\alpha_j$ , the eigenstates do. Since this will play a role in the results to be presented below, in figure 1 we have highlighted the  $k$ -dependent spin orientation in the  $x$ - $z$  plane of the local eigenstates, distinguishing the cases  $\alpha > 0$  and  $\alpha < 0$  by blue and red arrows, respectively. Furthermore, since in the quantum coherent limit the inhomogeneous solution is characterized by a given energy  $E$ , in each region one has to identify all four wavevectors corresponding to such energy, retaining both real wavevectors (propagating modes) and complex wavevectors (evanescent modes). In particular, the expression of the evanescent modes, which turn out to play an important role when matching the wavefunctions in different regions, leads to one further distinction between the weak Zeeman regime ( $2E_{\text{SO},j} < E_Z < 4E_{\text{SO},j}$ ) and the strong Zeeman regime ( $E_Z > 4E_{\text{SO},j}$ ). After performing such lengthy but straightforward classification of all eigenstates, whose technical details and results are reported in appendix A, the general solution at energy  $E$  is built up by matching the linear superpositions at each interface. Explicitly, at the  $j$ -th interface located at position  $x_j$  and separating two regions with RSOC values  $\alpha_j$  (on the left) and  $\alpha_{j+1}$  (on the right), the boundary



conditions are

$$\begin{cases} \hat{\Psi}(x_j^-) &= \hat{\Psi}(x_j^+) \\ \partial_x \hat{\Psi}(x_j^-) &= \partial_x \hat{\Psi}(x_j^+) - \frac{im^*}{\hbar^2} (\alpha_{j+1} - \alpha_j) \sigma_z \hat{\Psi}(x_j) \end{cases} \quad (9)$$

Then, by applying the scattering matrix formalism [69], where the external regions act like the leads and the inhomogeneous profile determines the scattering region, we compute the scattering matrix and determine the transmission coefficient  $T(E)$  for various inhomogeneous configurations. Details and examples are provided in appendix B. This enables us to determine how the low temperature linear conductance

$$G = \frac{e^2}{h} T(E_F) \quad (10)$$

depends on the RSOC and the Zeeman field, allowing for an electrical and magnetic tuning of the transport properties.

### 3. Two essential ingredients to observe effects of the RSOC sign

Because our purpose is to analyze the effect of the sign of the RSOC on transport properties, it is first worth pointing out some general conditions for this to be observed. We start by noting that the transmission coefficient is completely independent of a *global* sign change of the RSOC profile,  $\alpha(x) \rightarrow -\alpha(x)$ . Indeed the Hamiltonian (1) with a profile  $-\alpha(x)$  can be mapped back into the one with a profile  $+\alpha(x)$  through the transformation  $\hat{\Psi}(x) \rightarrow \sigma_x \hat{\Psi}(x)$ . This implies, for instance, that for a finite length NW with a homogeneous RSOC contacted two normal leads with vanishing RSOC, modelled with an inhomogeneous profile  $\alpha(x) = \alpha\theta(d/2 - |x|)$ , where  $\theta$  denotes the Heaviside function and  $d$  is the NW length, the conductance is independent of  $\text{sgn}(\alpha)$ . In particular, we note that the effect of Fano anti-resonances with vanishing transmission occurring in such a case for suitably chosen parameters [67, 70, 71] is completely insensitive to the sign of the RSOC in the NW.

Thus, a necessary condition for the effects of the RSOC sign to be observed is that the sign of the RSOC in a portion of the profile  $\alpha(x)$  changes with respect to the rest. However, it may not be sufficient. Compare for instance the uniform profile  $\alpha(x) \equiv \alpha_0$  and the inhomogeneous profile  $\alpha(x) = \alpha_0 \text{sgn}(x)$ , where the sign on the left of the origin is changed with respect to the one on the right. Despite the abrupt sign change of the RSOC, in the absence of the Zeeman field ( $h_{\perp} = 0$ ) the electron transmission is always perfect and equal to the case of a uniform profile. This can be straightforwardly deduced from the mapping described in section 2.1, since the potential equation (6) reduces to a mere homogeneous constant  $U_{SO} \equiv -m^* \alpha_0^2 / 2\hbar^2$ . In contrast, if  $h_{\perp} \neq 0$ , the term in the second line of equation (5) is present and the phase  $\phi_{SO}(x)$  in equation (4) depends on the sign of  $\alpha$ .

From these remarks, we conclude that the two essential ingredients to observe effects of the RSOC sign on electron transport are (i) a Zeeman field directed perpendicularly to the RSOC effective magnetic field and (ii) the presence of at least *two* regions with different RSOC value. This is what we shall consider in the following, focussing on the intrinsic transmission properties of the inhomogeneous RSOC. The

presence of spurious resistance due to non-ideal contacts with external electrodes can in principle be taken into account with the method outlined in appendix B. However, it depends on the specific metals used as electrodes and on the adiabaticity of the contacts [72], and it goes beyond the purpose of this paper.

#### 4. The single interface problem

We start by analyzing the transmission across an interface separating two regions with different RSOC, namely

$$\alpha(x) = \begin{cases} \alpha_L & \text{for } x < 0 \\ \alpha_R & \text{for } x > 0 \end{cases}. \quad (11)$$

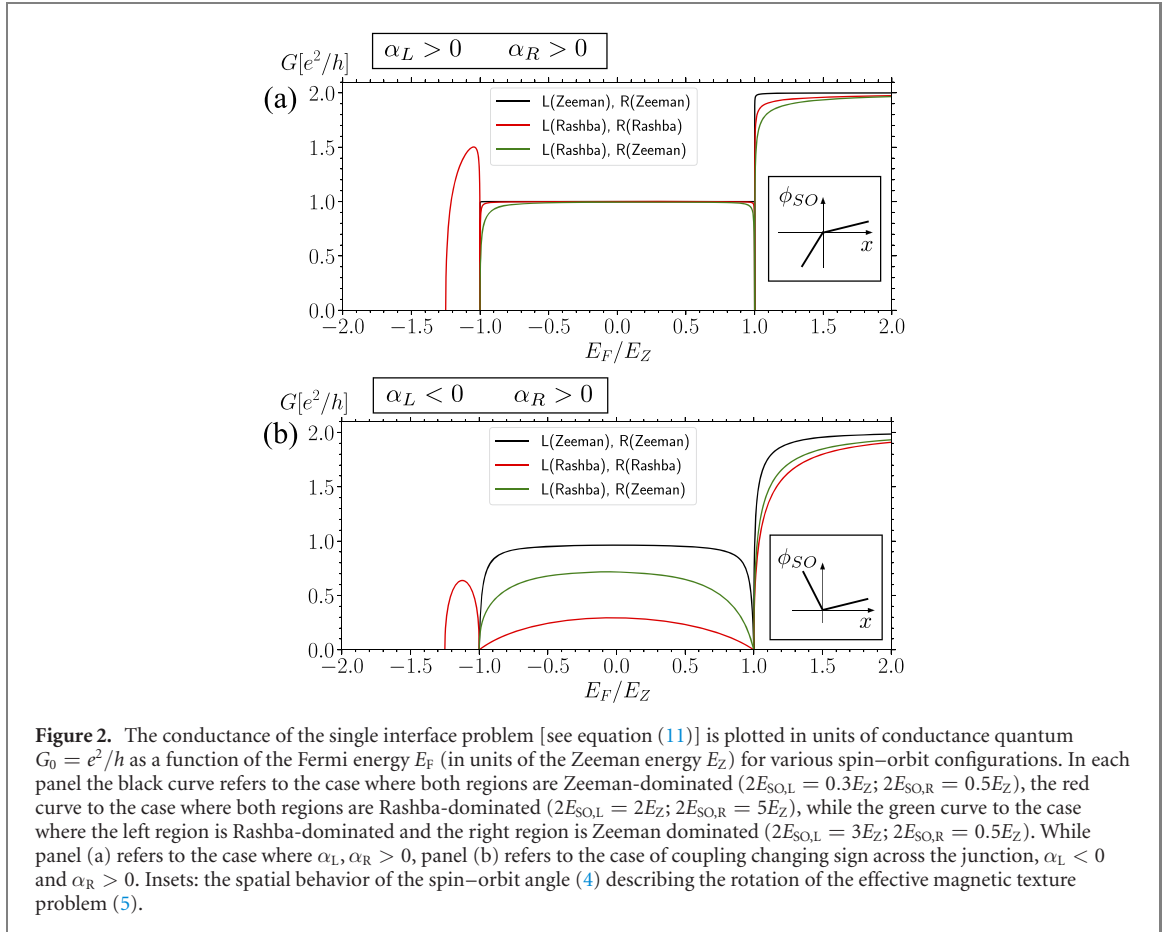
Depending on the strength of the RSOC, each interface side can be in the Rashba-dominated or in the Zeeman-dominated regime. After solving the scattering problem, as outlined in the appendix B, we have determined the transmission coefficient and the conductance from equation (10). Specifically, figure 2 shows the conductance  $G$ , in units of the conductance quantum  $G_0 = e^2/h$ , as a function of the Fermi energy  $E_F$ , in units of the Zeeman energy  $E_Z$ , for the three independent configurations: Zeeman–Zeeman, Rashba–Rashba, and Rashba–Zeeman [73]. In particular, figure 2(a) illustrates the case where the RSOC has the same sign in both sides. Recalling that the energy range  $|E_F| < E_Z$  corresponds to the magnetic gap (see figure 1), we first note that, when both sides are in the Rashba-dominated regime (red curve), transmission is possible also in the energy range below the magnetic gap, where it can also exceed  $G_0$ . This is because two propagating channels exist in the range  $E_{\min} < E < -E_Z$ , as one can see from the Mexican-hat shaped band in figure 1(a). At the energies  $E_F = \pm E_Z$  corresponding to the magnetic gap edges, the conductance of figure 2(a) exhibits two sharp anti-resonance suppression cusps, an effect similar to the one found in references [70, 71] in a NW coupled to two leads. We shall comment about this aspect at the end of this section. Apart from these features, one finds a practically perfect transmission, namely  $G = G_0$  when the Fermi energy lies inside the magnetic gap,  $|E_F| < E_Z$ , (one propagating channel) and  $G = 2G_0$  above the gap  $E > E_Z$  (two propagating channels), regardless of the specific regime configuration.

A different scenario emerges when the RSOC takes opposite signs across the interface, as shown in figure 2(b). In all configurations the conductance in the magnetic gap range  $|E_F| < E_Z$  remains roughly symmetric with respect to the midgap energy value  $E_F = 0$ . However, we note that, while the transmission is practically perfect when both sides are in the strong Zeeman regime (black curve), it reduces when one region enters the Rashba regime (green curve) and even more when both regions are Rashba-dominated (red curve). The different behavior of the conductance in the two panels (a) and (b) can be qualitatively understood through the mapping to the magnetic texture problem equation (5). In the present case of the profile equation (11) the rotation angle (4) of the magnetic field acquires the form

$$\phi_{\text{SO}}(x) = \frac{2m^*}{\hbar} \times \begin{cases} \alpha_R x & \text{for } x > 0 \\ \alpha_L x & \text{for } x < 0 \end{cases} \quad (12)$$

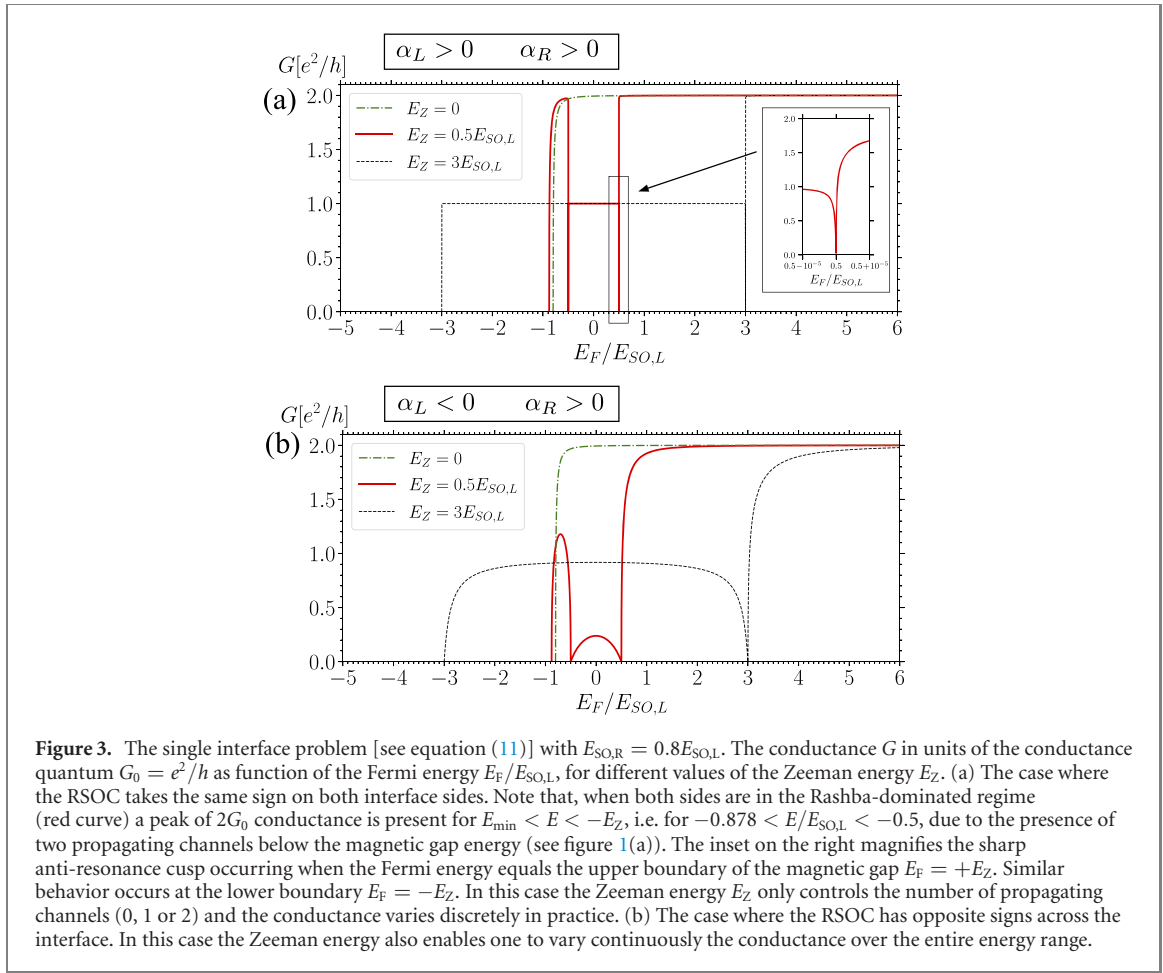
and its spatial behavior is depicted in the insets of the two panels of figure 2. If  $\alpha_L$  and  $\alpha_R$  have the same sign [inset of panel (a)], the incoming wavefunction can easily adapt to the change of slope of  $\phi_{\text{SO}}(x)$  from one side to the other by simply stretching or shrinking, since a coordinate rescaling  $x \rightarrow x\alpha_R/\alpha_L$  would compensate for the slope change. This leads to a very high transmission. In contrast, when  $\alpha_L$  and  $\alpha_R$  have opposite signs, an actual cusp appears in  $\phi_{\text{SO}}$  [inset of panel (b)], which cannot be merely removed by an affine coordinate transformation. It is therefore more difficult for the incoming wavefunction spinor to re-adapt to the profile on the other side of the interface. As long as the values of the RSOC are small (both regions in the Zeeman dominated regime) this effect is negligible, but when both regions enter the Rashba-dominated regime the mismatch becomes important and the transmission is suppressed.

The role of the RSOC sign can also be highlighted by considering the magnetic tuning of the conductance  $G$  in a Rashba interface where both sides are in the same regime. As an illustrative example of such situation, figure 3 describes the Fermi energy dependence of  $G$  for a junction with  $E_{\text{SO,R}}/E_{\text{SO,L}} = 0.8$ , for various values of the Zeeman energy  $E_Z$ . Specifically, panel (a) shows the case where the RSOC takes the *same* sign across the interface ( $\alpha_L, \alpha_R > 0$ ). When the magnetic field is absent (green dash-dotted curve) the conductance vanishes for  $E_F < -E_{\text{SO,R}}$  and then rapidly increases to  $2G_0$  for  $E_F > -E_{\text{SO,R}}$ . This is exactly

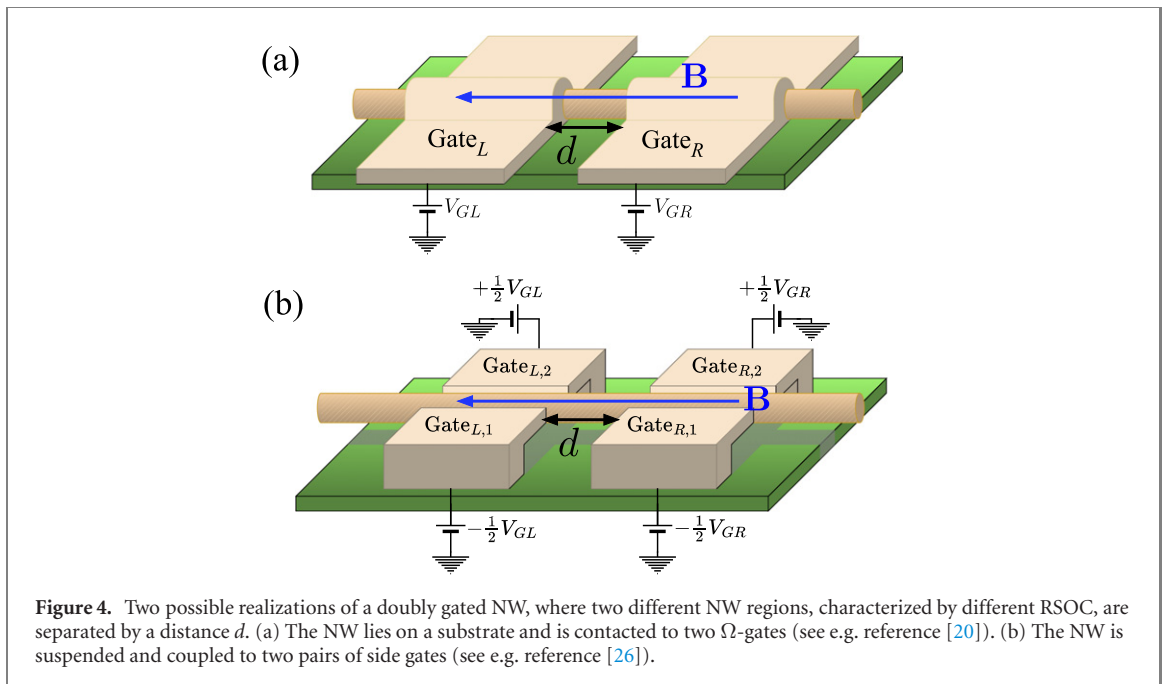


the same energy dependence as a spin-degenerate problem of transmission across a potential step ( $-E_{SO,L} - E_{SO,R}$ ), as argued invoking the mapping described in section 2.1. In contrast, when a weak Zeeman field is introduced (red solid curve), the conductance gets suppressed down to  $G_0$  for  $|E_F| < E_Z$  due to the magnetic gap opening that leaves only one propagating channel. Again, very narrow cusps with vanishing conductance appear at Fermi energies corresponding to the magnetic gap boundaries  $E_F = \pm E_Z$  (one of them is highlighted in the inset on the left). For a stronger Zeeman field (black dashed line) both sides enter the Zeeman-dominated regime and the conductance acquires a step-like behavior characterizing the number of propagating channels (0, 1 or 2). Thus, in this case of equal RSOC signs, the Zeeman energy in practice controls only the number of such channels, i.e. the value at which the jump occurs. Figure 3(b) instead describes the case of *opposite* RSOC sign across the interface, i.e.  $\alpha_L < 0$  and  $\alpha_R > 0$ . For vanishing Zeeman field the conductance is insensitive to the sign of the RSOC, so that the green dash-dotted curve is exactly equal to the one obtained in figure 3(a). Again, exploiting the mapping (3) described in section 2.1, one can see that in such situation only the potential (6) is present. In contrast, when the Zeeman field is introduced, the sign of the RSOC matters and the behavior strongly differs from panel (a). The conductance varies continuously as a function of the Fermi energy. In this case the Zeeman energy  $E_Z$  determines not only the location of the suppression cusps at the magnetic gap edges, but also the magnitude of  $G$  in the entire energy range. In particular, when the NW is in the Rashba dominated regime (red curve), the conductance is significantly suppressed inside and below the magnetic gap.

*Anti-resonances in the conductance.* We conclude this section by a comment about the anti-resonance cusps with vanishing conductance displayed in figures 2 and 3. We emphasize that their presence is not due to the RSOC sign change across the interface, as they do exist both in the case of equal and opposite RSOC signs, and turn out to be much sharper in the former case [see inset of figure 3(a)]. Although this effect is thus generic and not strictly related to the main focus of our paper, for the sake of completeness in the presentation of our results, a brief discussion about their origin is in order. We recall that the existence of vanishing conductance dips, typically close in energy to resonance peaks of perfect transmission, is known to occur in the case of a NW contacted to leads [70, 71], and is attributed to the fact that the RSOC present in the centrally confined NW region leads to a spin misalignment of its bound states with respect to the outer leads with continuum spectrum, causing one bound state to be strongly coupled to the continuum, while the other one is very weakly coupled. With respect to the configuration analyzed in references



[70, 71], our case of a single interface between two RSOC regions exhibits two differences: (i) here, within the energy gap, there are no bound states at the interface [74]; (ii) the anti-resonances with vanishing transmission are always pinned at the boundaries  $E = \pm E_Z$  of the magnetic gap. Their origin can be argued as follows. Within the energy range  $|E| < E_Z$  of the magnetic gap, each side of the interface is characterized by propagating modes (see figure 1), whose spin orientations lying in the  $x$ - $z$  spin plane are in general misaligned, because the RSOC takes different values across the interface. However, one also has evanescent modes originating from the band spin-splitting in the magnetic gap [see figure 8(b) and figures 9(b) and (c) in appendix A], whose spin orientation lies in the  $x$ - $y$  spin plane. On each interface side the wavefunction is thus a superposition of both propagating and evanescent modes. Although the transmission is carried by the propagating modes only, the evanescent modes *indirectly* affect the transmission because they contribute to realize the wavefunction matching equation (9) at the interface. Effectively, one could consider the two RSOC regions as ‘leads’ with (massless) propagating modes  $\Psi_{pr}$  with misaligned spins, which are coupled to (massive) evanescent modes  $\Psi_{ev} = \xi e^{\pm\kappa+x}$  localized at the interface, whose spinor  $\xi$  effectively performs the spin rotation, thereby favoring the transmission [75]. Of course, in the case of equal RSOC signs, the misalignment of the propagating modes is less pronounced than in the case of opposite RSOC signs, and this is why for  $|E| < E_Z$  the transmission is typically higher in figure 2(a) than in 2(b). However, as the energy approaches (say) the upper edge of the magnetic gap,  $E \rightarrow E_Z$ , each evanescent mode becomes the state related to the minimum of the upper band (see figure 1): its spin gets locked along  $x$  and its decay lengthscale diverges. This makes it effectively unable to guarantee a finite transmission, since a spatially uniform mode has a vanishing spatial overlap with a propagating mode. The transmission thus vanishes with a cusp behavior because the evanescent mode wavevector  $\kappa_+$  vanishes with an infinite slope as a function of energy  $E \rightarrow E_Z$ . To a more quantitative level, one can see that in such a limit  $\Psi_{ev}$  can contribute to the first interface matching equation (9) only with a spin along  $x$ , and its contribution to the spatial derivative in the second equation (9) vanishes. It turns out that the only way to realize a wavefunction matching of both equation (9) at the interface is to have a totally reflected mode, as one can verify by plotting the wavefunction profile (not shown here). A similar effect occurs at the lower magnetic gap edge  $E \rightarrow -E_Z$  when the region is in the Rashba-dominated regime, since the evanescent mode becomes the state related to the local maximum of the lower band (see figure 1).



## 5. The doubly gated nanowire

The analysis of the single interface case carried out in the previous section indicates that the conductance heavily depends on the relative sign between the two RSOC regions. However, a sharp separation between the two RSOC regions is in fact an idealization. In a realistic NW setup, where the RSOC can be locally controlled by different gates, a finite distance  $d$  separates the gates, as shown in the configurations sketched in figure 4. In particular, panel (a) describes a realization with a NW deposited on a substrate and covered by two  $\Omega$ -gates [20]. In this kind of setup the NW is usually separated from the metallic gate by a thin (few nm) dielectric with high relative dielectric constant, which—at a given gate voltage—enhances the interface field causing the RSOC [32, 76]. In contrast, figure 4(b) illustrates a suspended NW coupled to two pairs of side gates with the advantage of strongly reducing the presence of defects [26]. In both cases the gate voltages control the magnitude and the sign of the RSOC.

We now want to take into account the finite size  $d$  of the central region separating the two gated NW regions, which was neglected in the preliminary analysis of section 4. For definiteness we shall assume that the RSOC in the central region is negligible, so that it is in the strongly Zeeman-dominated regime, and we shall adopt the following profile

$$\alpha(x) = \begin{cases} \alpha_L & \text{for } x < -d/2 \\ 0 & \text{for } |x| < d/2 \\ \alpha_R & \text{for } x > d/2 \end{cases} \quad (13)$$

Moreover, we shall set the RSOC to be positive in the right region ( $\alpha_R > 0$ ), while for the left region we will consider both positive and negative sign of  $\alpha_L$ .

In figure 5 we analyze the conductance  $G$  as a function of the Fermi energy over the entire spectrum. We focus on the case where the two regions are both in the Rashba-dominated regime. The two spin-orbit energies equation (7) identify two spin-orbit wavevectors

$$k_{\text{SO},j} = \frac{\sqrt{2m^*E_{\text{SO},j}}}{\hbar} = \frac{m^*|\alpha_j|}{\hbar^2} \quad j = L, R, \quad (14)$$

and the related spin-orbit lengths  $k_{\text{SO},j}^{-1}$ . For definiteness we take  $E_{\text{SO},L} = 2E_{\text{SO},R}$  and express the gate separation  $d$  in units of the shorter spin-orbit length  $k_{\text{SO},L}^{-1}$ . In particular, figure 5(a) illustrates the result for a short gate separation: the conductance is practically perfect inside the magnetic gap when the two regions have equal RSOC sign (black curve), whereas it is suppressed when the two regions have opposite RSOC

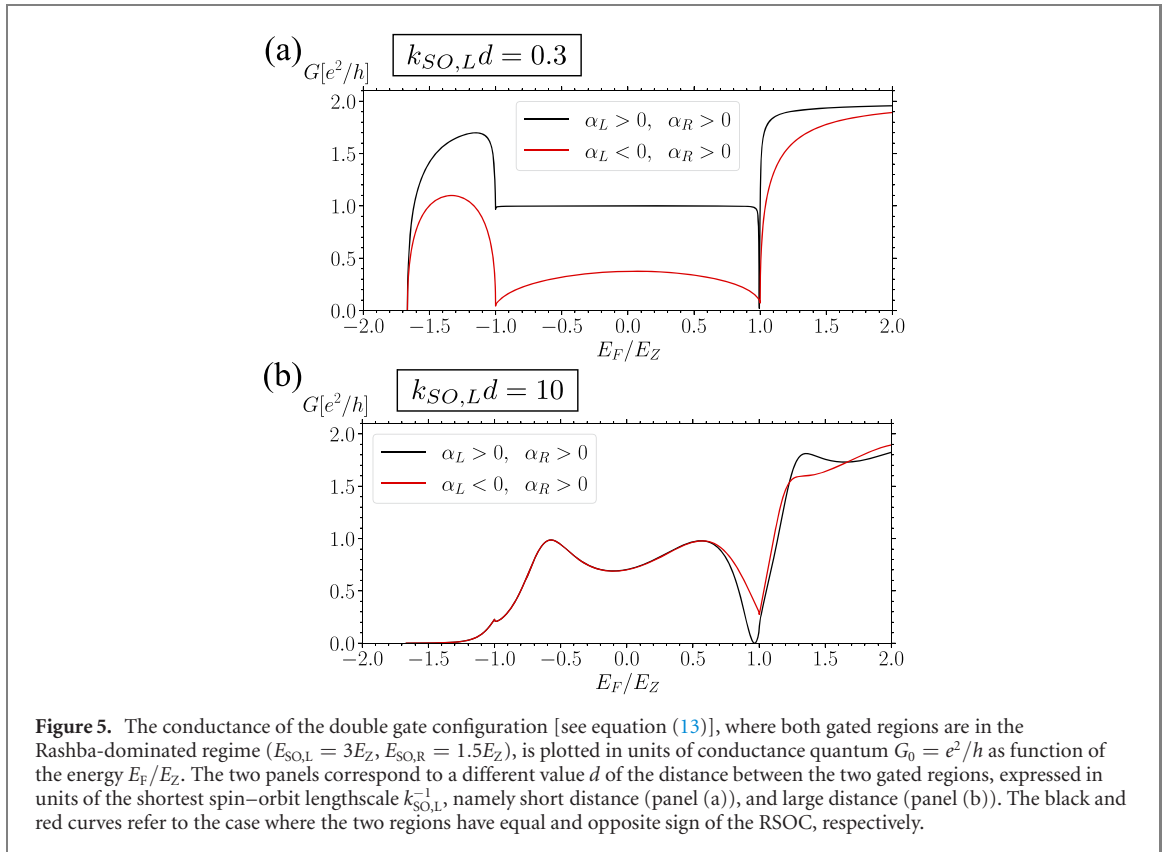
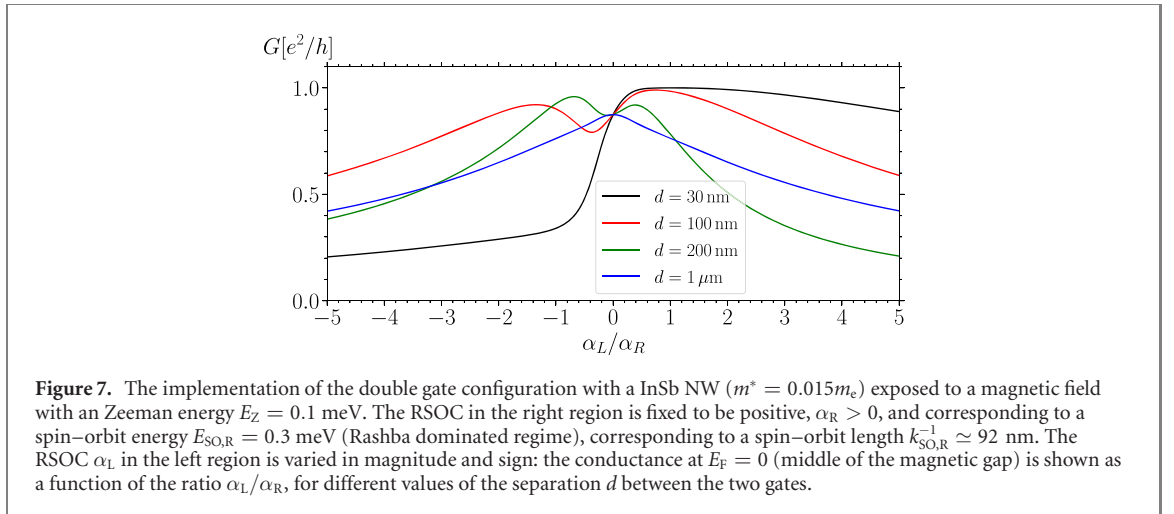
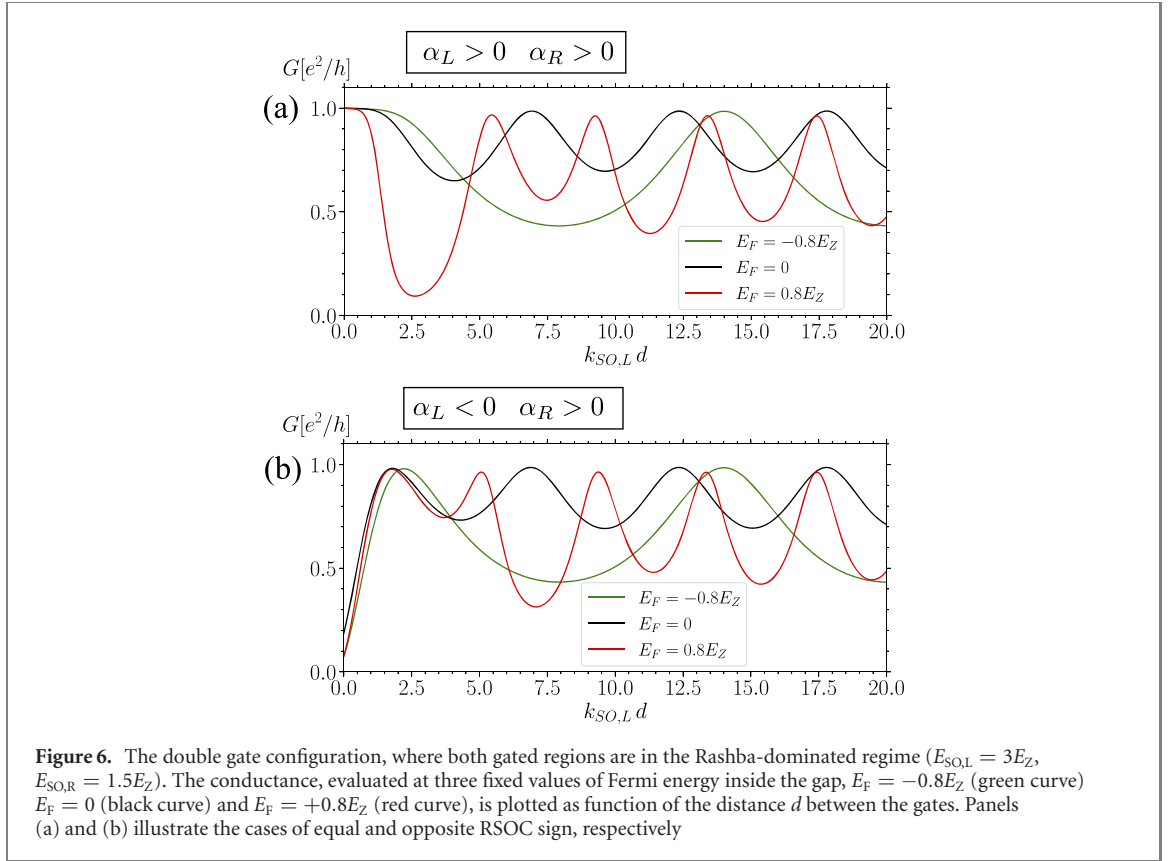


**Figure 5.** The conductance of the double gate configuration [see equation (13)], where both gated regions are in the Rashba-dominated regime ( $E_{\text{SO,L}} = 3E_Z$ ,  $E_{\text{SO,R}} = 1.5E_Z$ ), is plotted in units of conductance quantum  $G_0 = e^2/h$  as function of the energy  $E_F/E_Z$ . The two panels correspond to a different value  $d$  of the distance between the two gated regions, expressed in units of the shortest spin-orbit lengthscale  $k_{\text{SO,L}}^{-1}$ , namely short distance (panel (a)), and large distance (panel (b)). The black and red curves refer to the case where the two regions have equal and opposite sign of the RSOC, respectively.

sign (red curve). Moreover, transmission is almost symmetric in energy and flat around the middle of the magnetic gap ( $E = 0$ ). The result does not deviate much from the one obtained in figure 2 for the ideal  $d \rightarrow 0$  limit. However, for large gate separation [see figure 5(b)], the difference between the two cases of equal or opposite RSOC signs is strongly reduced, except for a small difference near the gap edge  $E/E_Z = +1$ . This is due to the fact that, for larger separation  $d$ , the electron spin has a spatial room to re-adapt to the different orientation imposed by the opposite RSOC sign. We also note the cusps with vanishing conductance discussed in the single interface problem are modified by the finite distance  $d$  between the gates. First, the effect of vanishing conductance may still be present, but it occurs at values of Fermi energy that can slightly differ from the magnetic gap boundaries, as is visible e.g. in the black curve of figure 5(b), near the upper magnetic gap boundary  $E_F = +E_Z$ . This makes the doubly gated NW configuration similar to the configuration of a NW contacted to leads [70, 71]. Second, the cusp behavior might occur at a finite conductance value. This can be the case even for a short distance  $d$  [see figure 5(a)] and is especially visible near the lower magnetic gap boundary  $E_F = -E_Z$ . In this case, only for very short distance ( $k_{\text{SO,L}}d < 0.01$ ) one recovers the vanishing conductance of the single interface problem.

Figure 6 illustrates how the conductance, evaluated at three different Fermi energy values inside the magnetic gap, behaves as a function of the distance  $d$  between the two gates. At short distance,  $k_{\text{SO,L}}d \ll 1$ , the behavior of  $G$  strongly depends on whether the signs of the two RSOCs are equal [panel (a)] or opposite [panel (b)]: in the former case it is independent of the distance  $d$  for all energy values ( $G \cong G_0$ ), while in the latter case it linearly grows with the distance and it is small ( $G \ll G_0$ ). As the distance  $d$  becomes of the order of the spin-orbit length,  $k_{\text{SO,L}}d \sim 1$ , in both cases the conductance exhibits a crossover to an oscillatory behavior. This originates from the fact that at the boundaries of the central region part of the electron wave is reflected, giving rise to interference conditions that depend on the distance  $d$ . Because the electron wavelength depends on the Fermi energy, such oscillatory pattern depends on  $E_F$  too, as one can see from the different period characterizing the various curves. Notably, for large distance  $k_{\text{SO,L}}d \gg 1$ , such oscillatory behavior becomes independent of the relative RSOC signs of the two regions, as can be appreciated by comparing panels (a) and (b).

*Implementation with InSb NWs.* Let us now consider a specific implementation of the setup of figure 4 with a InSb NW, with effective mass  $m^* = 0.015m_e$  and  $g$ -factor  $g \simeq 50$ , exposed to a magnetic field corresponding to a Zeeman energy  $E_Z = 0.1$  meV. For definiteness, for the RSOC in the right region we



have fixed a positive value  $\alpha_R \simeq 0.552 \text{ eV } \text{\AA} > 0$  corresponding to a spin-orbit energy  $E_{SO,R} = 0.3$  meV  $= 3E_Z$ , so that the right region is in the Rashba-dominated regime. Then, by varying  $\alpha_L$  over a broad range of positive and negative values, we have analyzed how the conductance in the middle of the magnetic gap ( $E_F = 0$ ) depends on the ratio  $\alpha_L/\alpha_R$ . The result is plotted in figure 7 for four different values of the distance  $d$  between the two gates, which can be compared to the reference lengthscale given by the fixed spin-orbit length of the right-side is  $k_{SO,R}^{-1} \simeq 92$  nm. As one can see, when  $d$  is much shorter than the latter scale (black curve) the conductance  $G$  exhibits a strongly asymmetric curve as a function of  $\alpha_L/\alpha_R$ . In this case  $G$  depends only weakly on the magnitude of the RSOC, and strongly on the sign. Indeed a sign switch of  $\alpha_L$  from positive to negative changes the transmission from high to low values. In contrast, when  $d$  becomes of the order of the spin-orbit length (red and green curves), the asymmetry of the curve gradually softens and eventually, for a large separation  $d = 1$   $\mu$ m (blue curve), the conductance exhibits a completely symmetric Lorentzian-like behavior as a function of  $\alpha_L/\alpha_R$ . In this regime only the magnitude of the RSOC determines the conductance, while the relative sign of the RSOC plays no role.

*The helical limit.* We conclude this section by a comment about the helical limit. As is well known, in the strongly Rashba-dominated regime,  $E_{\text{SO}} \gg E_Z$ , the propagating states in the magnetic gap are helical, i.e. they exhibit a locking between the propagation direction [1, 2, 53–57], similarly to the edge states of a 2D topological insulator. Importantly, in a NW the helicity is controlled by the sign of the RSOC. Explicitly, if  $\alpha > 0$  right-movers are characterized by spin- $\uparrow$  and left-movers by spin- $\downarrow$ , while the opposite occurs for  $\alpha < 0$ , as is clear from the blue/red arrows in figure 1(a). This opens up the possibility to conceive transport configurations that would be quite hard in 2D topological insulators. Let us now consider the inhomogeneous setup sketched in figure 4 in the limit where both gated regions are set to the strongly Rashba-dominated and exhibit opposite RSOC signs. This implements a peculiar setup, namely a junction of helical states with opposite helicity, the so called Dirac paradox. As is well known, for a NW with homogeneous RSOC, the low energy transport within the magnetic gap, i.e. in the energy range  $|E_F| \ll E_Z$ , is well captured by a massless Dirac model describing the helical states. One may thus wonder whether in such energy window the behavior of the conductance for the inhomogeneous setup of figure 4 could be deduced from the low energy massless Dirac models. This is indeed the case when the RSOC takes the same sign in both gated regions: the low energy effective theory is well captured by two massless Dirac models with the same helicity, one on each region, and one recovers a perfect transmission at low energy [77]. However, in the case of opposite RSOC signs, the customary massless Dirac models are not sufficient to describe the low-energy transport. Instead it is possible to show [75] that additional massive Dirac modes have to be included on each side to correctly account for the low-energy behavior at  $|E_F| \ll E_Z$ . Although in such energy window these modes are evanescent and carry no current directly, they do contribute to the current indirectly by favoring the correct wavefunction matching at the interface. The transmission thus depends on the parameter  $k_{\text{SO}}d$  in a non-monotonous way [75], in agreement with the more general results presented here.

## 6. Conclusions

In conclusion, in this paper we have analyzed the effects of the sign of the RSOC on electron transport in a one-dimensional electron channel in the quantum coherent regime. In the case of a NW with homogeneous RSOC and contacted to two electrodes, despite the spin orientation of the eigenstates depends on the sign of the RSOC (see figure 1), we have shown that the transport properties are independent of  $\text{sgn}(\alpha)$ . In fact, in section 3 we have identified two essential ingredients for the effects of the sign to be observed, namely the presence of (i) at least two regions with different RSOC and (ii) an additional Zeeman field that is non collinear with the effective RSOC magnetic field. In section 4 we have first analyzed the electron transport across an ideal interface separating two regions with different RSOC. We have shown that, when the sign of the RSOC is the same in both regions, the transmission is practically perfect, *regardless* of the regimes (Rashba- or Zeeman-dominated) of the two regions [see figure 2(a)]. In this case the magnetic field essentially determines the number of conducting channels and the conductance can be tuned to integer values of the conductance quantum [see figure 3(a)]. The scenario changes when the RSOC exhibits opposite signs at the two interface sides. In particular, while transmission remains extremely good when both regions are in the Zeeman regime, it reduces when one of the two regions enters the Rashba regime, and it gets suppressed when both regions are in the Rashba regime [see figure 2(b)]. In this case, the conductance can be continuously tuned by varying the Zeeman field [see figure 3(b)].

Then, in section 5 we have considered a more realistic NW setup, where two different RSOC regions are realized by coupling the NW to various gates (see figure 4), and we have taken into account the finite distance  $d$  between the gates. The impact of the sign is quite different in the two regimes of small and large separation  $d$  (see figure 5). Indeed, by analyzing the conductance as a function of the separation  $d$  (see figure 6), we have found that in the regime of short separation the conductance strongly depends on the relative RSOC signs, namely for equal signs one has  $G \cong G_0$ , roughly independently of  $d$ , while for opposite signs one has  $G \ll G_0$  growing linearly with  $d$ . In contrast, as the separation becomes comparable with the spin-orbit length, the conductance exhibits a crossover to an oscillatory behavior, originating from the quantum interference of the electron backscattering of the ends of the separation region. In particular, for large separation ( $k_{\text{SO},L}d \gg 1$ ) such oscillatory behavior becomes independent of the relative RSOC signs.

Furthermore, we have considered a specific implementation of the setup of figure 4 with InSb NWs, for four realistic values of separation  $d$  between the gates. Focussing on the midgap conductance  $G$  of the setup as a function of the ratio  $\alpha_L/\alpha_R$  between the two RSOCs (see figure 7), we have been able to identify the conditions where  $G$  is mainly determined by the sign or by the magnitude of the RSOC. In particular, for a short separation  $d = 30$  nm, the conductance mainly depends on the relative RSOC signs, and one can tune

$G$  from a small to a high fraction of  $e^2/h$  by varying the ratio  $\alpha_L/\alpha_R$  from negative to positive values (black curve in figure 7). In this regime, the RSOC sign thus represents an actual additional knob to switch on/off the electron current through the NW. In contrast, for a large separation  $d = 1 \mu\text{m}$ , the conductance becomes insensitive to the sign of  $\alpha_L/\alpha_R$  (see blue curve in figure 7) and is mainly dependent on the RSOC magnitude only. Finally, we have discussed that, for the particular range of small energies  $|E_F| \ll E_Z$  inside the magnetic gap, our findings are in agreement with the low-energy Dirac theory: while in the case of two regions with equal RSOC signs the low-energy electron transport is well described by massless Dirac modes, in the case of opposite RSOC signs this is not the case, and additional massive Dirac modes have to be included.

A potentially interesting future development of this work is to extend the analysis of electron transport through the doubly gated NW to the case of ac gate voltages [63, 78–81], where two time-dependent RSOC are induced along the NW. Work is in progress along these lines.

## Acknowledgments

We are thankful to Lorenzo Rossi for fruitful discussions.

## Data availability statement

The data that support the findings of this study are available upon reasonable request from the authors.

## Appendix A. Classification of NW eigenstates

As mentioned in the main text, the solution of the inhomogeneous RSOC problem is built by suitably matching the wavefunctions of each piecewise homogeneous NW region. To this purpose, for each energy value  $E$ , one has to classify all eigenstates (both propagating and evanescent) of a given NW region with RSOC  $\alpha_j$ . This appendix is meant to provide this classification. In order to make the notation lighter, we shall use in this section  $\alpha_j \rightarrow \alpha$  and  $E_{\text{SO},j} \rightarrow E_{\text{SO}}$ .

*Propagating states.* Let us start from the propagating modes  $\psi(x) = \chi \exp[\pm ikx]$ , where  $\chi$  is a  $2 \times 1$  spinor. Denoting  $\varepsilon_k^0 = \hbar^2 k^2 / 2m^*$  and inverting the energy spectra  $E_{1,2}(k) = \varepsilon_k^0 \mp \sqrt{E_Z^2 + (\alpha k)^2}$  of the two bands ( $\beta = 1, 2$ ) in favour of the energy  $E$ , there are *a priori* four wavevectors for each value of  $E$ , namely two positive ones,  $k_{\pm}(E)$ , and two negative ones  $-k_{\pm}(E)$ , where

$$k_{\eta}(E; \alpha) = \frac{\sqrt{2m^*}}{\hbar} \sqrt{E + 2E_{\text{SO}} + \eta \sqrt{4EE_{\text{SO}} + 4E_{\text{SO}}^2 + E_Z^2}} \quad \eta = \pm. \quad (\text{A1})$$

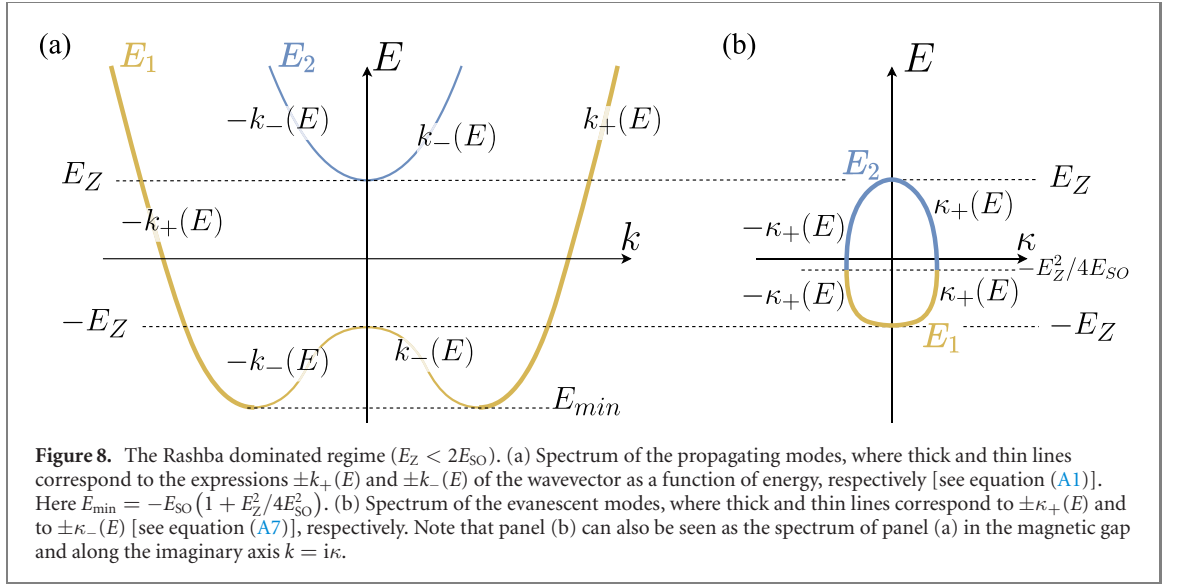
This can explicitly be seen from figure 8(a) for the Rashba-dominated regime and in figure 9(a) for the Zeeman-dominated regime, where  $k_+$  and  $k_-$  are distinguished by thick and thin curves, respectively. However, only real wavevectors ( $k_{\eta} \in \mathbb{R}$ ) actually describe propagating modes and must be retained. For these wavevectors, the magnitude  $v = \hbar^{-1} |\partial_k E|$  of the group velocity is expressed as a function of energy as

$$v_{\eta}(E; \alpha) = \frac{\hbar k_{\eta}(E; \alpha)}{m^*} \frac{\sqrt{4EE_{\text{SO}} + 4E_{\text{SO}}^2 + E_Z^2}}{\left| 2E_{\text{SO}} + \eta \sqrt{4EE_{\text{SO}} + 4E_{\text{SO}}^2 + E_Z^2} \right|} \quad \eta = \pm. \quad (\text{A2})$$

For each wavevector related to the energy  $E$ , the spinor  $\chi$  acquires a different expression depending on the band  $\beta$ . Explicitly, the two eigenvectors of the lower band ( $\beta = 1$ ) and the upper band ( $\beta = 2$ ) are

$$\chi_1(\pm k_{\eta}(E; \alpha)) = \begin{pmatrix} \cos\left(\frac{\theta(\pm k_{\eta}(E; \alpha))}{2}\right) \\ \sin\left(\frac{\theta(\pm k_{\eta}(E; \alpha))}{2}\right) \end{pmatrix} \quad (\text{A3})$$

$$\chi_2(\pm k_{\eta}(E; \alpha)) = \begin{pmatrix} -\sin\left(\frac{\theta(\pm k_{\eta}(E; \alpha))}{2}\right) \\ \cos\left(\frac{\theta(\pm k_{\eta}(E; \alpha))}{2}\right) \end{pmatrix} \quad (\text{A4})$$



respectively, where

$$\cos\left(\frac{\theta(\pm k_\eta(E; \alpha))}{2}\right) = \sqrt{\frac{1}{2} \left( 1 \pm \operatorname{sgn}(\alpha) \frac{\sqrt{4E_{S0}(E + 2E_{S0}) + \eta 4E_{S0} \sqrt{4EE_{S0} + 4E_{S0}^2 + E_Z^2}}}{\sqrt{4EE_{S0} + 4E_{S0}^2 + E_Z^2 + \eta 2E_{S0}}} \right)} \quad (\text{A5})$$

$$\sin\left(\frac{\theta(\pm k_\eta(E; \alpha))}{2}\right) = \operatorname{sgn}(h_\perp) \sqrt{\frac{1}{2} \left( 1 \mp \operatorname{sgn}(\alpha) \frac{\sqrt{4E_{S0}(E + 2E_{S0}) + \eta 4E_{S0} \sqrt{4EE_{S0} + 4E_{S0}^2 + E_Z^2}}}{\sqrt{4EE_{S0} + 4E_{S0}^2 + E_Z^2 + \eta 2E_{S0}}} \right)} \quad (\text{A6})$$

The eigenstates (A3) and (A4) identify a spin lying in the  $x$ - $z$  plane and forming an angle  $\theta$  with the  $z$ -axis. This enables one to obtain the pattern of spin-orientation in the two bands in figure 1.

*Evanescent states.* One can proceed in a similar way for the evanescent modes  $\psi(x) = \xi \exp[\pm \kappa x]$ , where  $\xi$  is a spinor. Their spectrum  $E_{1,2}(\kappa) = -\varepsilon_\kappa^0 \mp \sqrt{E_Z^2 - (\alpha\kappa)^2}$  consists of two bands ( $\beta = 1, 2$ ) touching at the energy  $E_{\min} = -E_Z^2/4E_{S0}$  for  $|\kappa| = E_Z/|\alpha|$ , as depicted in figure 8(b) for the Rashba-dominated regime and in figures 9(b) and (c) for the weak and strong Zeeman regime, respectively. When inverting the spectrum in favour of energy, one obtains

$$\kappa_\eta(E; \alpha) = \frac{\sqrt{2m^*}}{\hbar} \sqrt{-E - 2E_{S0} + \eta \sqrt{4EE_{S0} + 4E_{S0}^2 + E_Z^2}} \quad \eta = \pm \quad (\text{A7})$$

and the spinors acquire the form

$$\xi_1(\pm \kappa_\eta(E; \alpha)) = \frac{1}{\sqrt{2}} \begin{pmatrix} e^{\mp i \arctan(\sinh(\theta(\kappa_\eta(E; \alpha))))} \\ 1 \end{pmatrix} \quad (\text{A8})$$

$$\xi_2(\pm \kappa_\eta(E; \alpha)) = \frac{1}{\sqrt{2}} \begin{pmatrix} -e^{\pm i \arctan(\sinh(\theta(\kappa_\eta(E; \alpha))))} \\ 1 \end{pmatrix} \quad (\text{A9})$$

where

$$\sinh(\theta(\kappa_\eta(E; \alpha))) = \operatorname{sgn}(\alpha) \frac{\sqrt{-4E_{S0}(E + 2E_{S0}) + \eta 4E_{S0} \sqrt{4EE_{S0} + 4E_{S0}^2 + E_Z^2}}}{\sqrt{4EE_{S0} + 4E_{S0}^2 + E_Z^2 - \eta 2E_{S0}}} \quad (\text{A10})$$

Note that, differently from the spinors of the propagating modes, the eigenstates (A8) and (A9) identify a spin lying in the  $x$ - $y$  plane.

*Three possible regimes.* Depending on the local value of  $E_{S0}$  and  $E_Z$ , the NW region can be in three possible regimes, namely Rashba-dominated ( $2E_{S0} > E_Z$ ), weak Zeeman regime ( $2E_{S0} < E_Z < 4E_{S0}$ ) and

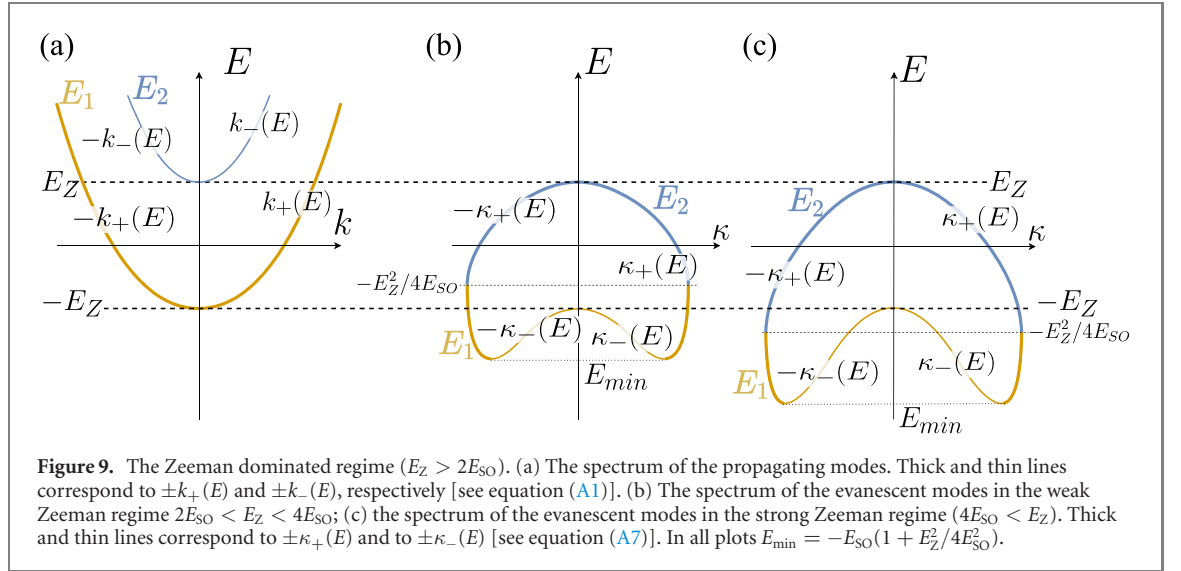


**Table 1.** Eigenstates of the NW in the Rashba dominated regime ( $2E_{SO} > E_Z$ ). For the propagating modes the wavevectors  $k_{\pm}$  are given in equation (A1), the velocities in equation (A2) and the spinors  $\chi_{1,2}$  in equations (A3) and (A4), while for the evanescent modes the wavevectors  $\kappa_{\pm}$  are given in equation (A7) and the spinors  $\xi_{1,2}$  are given in equations (A8) and (A9).

Rashba dominated regime ( $2E_{SO} > E_Z$ ) ( $E_{min} = -E_{SO}(1 + E_Z^2/4E_{SO}^2)$ ).			
Energy range	Propagating modes	Velocity	Evanescent modes
$E_{min} < E < -E_Z$	4 propagating states $\chi_1(\pm k_-(E))e^{\pm ik_-(E)x}$ $\chi_1(\pm k_+(E))e^{\pm ik_+(E)x}$ $[k_{\pm}(E) \in E_1 \text{ band}]$	$\mp v_-(E)$ $\pm v_+(E)$	No evanescent mode
$-E_Z < E < -\frac{E_Z^2}{4E_{SO}}$	2 propagating states $\chi_1(\pm k_+(E))e^{\pm ik_+(E)x}$ $[k_+(E) \in E_1 \text{ band}]$	$\pm v_+(E)$	$\xi_1(\pm \kappa_+(E))e^{\pm \kappa_+(E)}$ $[\kappa_+(E) \in E_1 \text{ band}]$
$-\frac{E_Z^2}{4E_{SO}} < E < E_Z$	2 propagating states $\chi_1(\pm k_+(E))e^{\pm ik_+(E)x}$ $[k_+(E) \in E_1 \text{ band}]$	$\pm v_+(E)$	$\xi_2(\pm \kappa_+(E))e^{\pm \kappa_+(E)}$ $[\kappa_+(E) \in E_2 \text{ band}]$
$E_Z < E$	4 propagating modes $\chi_2(\pm k_-(E))e^{\pm ik_-(E)x}$ $\chi_1(\pm k_+(E))e^{\pm ik_+(E)x}$ $[k_+(E) \in E_1 \text{ band}]$ $[k_-(E) \in E_2 \text{ band}]$	$\pm v_-(E)$ $\pm v_+(E)$	No evanescent mode

strong Zeeman regime ( $E_Z > 4E_{SO}$ ). For each of these regimes, there are various energy ranges where the eigenstates acquire different expressions. In table 1 we have summarized the result for the Rashba-dominated regime. In particular, propagating states exist for  $E > E_{min}$ , as can be seen from figure 8(a). Their wavevectors are given by equation (A1), the spinors  $\chi_1$  and  $\chi_2$ , related to the lower and upper band, respectively, are given in equations (A3) and (A4), while the velocities are given in equation (A2). In contrast, evanescent modes exist for  $|E| < E_Z$ , as shown in figure 9(a), their wavevectors are given in equation (A7), and the related spinors, related to the upper and lower band, are given in equations (A8) and (A9).

As far as the Zeeman-dominated regime is concerned ( $E_Z > 2E_{SO}$ ), propagating modes exist for  $E > -E_Z$  (see figure 8(b)), while evanescent modes exist for  $E_{min} < E < E_Z$ . However, the explicit expression and type (upper/lower band) of the NW states also depends whether the NW is in the weak Zeeman subregime ( $2E_{SO} < E_Z < 4E_{SO}$ ) or in the strong Zeeman subregime ( $4E_{SO} < E_Z$ ), as shown in figures 9(b) and (c). The expressions of eigenstates in the weak and strong Zeeman regimes are summarized in tables 2 and 3, respectively.

**Table 2.** Eigenstates of the NW in the weak Zeeman regime ( $2E_{SO} < E_Z < 4E_{SO}$ ). The meaning of symbols is the same as in table 1.

Weak Zeeman regime ( $2E_{SO} < E_Z < 4E_{SO}$ )			
Energy range	Propagating modes	Velocity	Evanescent modes
$-E_{SO} \left(1 + \frac{E_Z^2}{4E_{SO}^2}\right) < E < -E_Z$	No propagating states		$\xi_1(\pm\kappa_+(E))e^{\pm\kappa_+(E)x}$ $\xi_1(\pm\kappa_-(E))e^{\pm\kappa_-(E)x}$ [ $\kappa_{\pm}(E) \in E_1$ band]
$-E_Z < E < -\frac{E_Z^2}{4E_{SO}}$	2 propagating states $\chi_1(\pm k_+(E))e^{\pm ik_+(E)x}$ [ $k_+(E) \in E_1$ band]	$\pm v_+(E)$	$\xi_1(\pm\kappa_+(E))e^{\pm\kappa_+(E)x}$ [ $\kappa_+(E) \in E_1$ band]
$-\frac{E_Z^2}{4E_{SO}} < E < E_Z$	2 propagating states $\chi_1(\pm k_+(E))e^{\pm ik_+(E)x}$ [ $k_+(E) \in E_1$ band]	$\pm v_+(E)$	$\xi_2(\pm\kappa_+(E))e^{\pm\kappa_+(E)x}$ [ $\kappa_+(E) \in E_2$ band]
$E > E_Z$	4 propagating states $\chi_2(\pm k_-(E))e^{\pm ik_-(E)x}$ $\chi_1(\pm k_+(E))e^{\pm ik_+(E)x}$ [ $k_-(E) \in E_2$ band] [ $k_+(E) \in E_1$ band]	$\pm v_-(E)$ $\pm v_+(E)$	No evanescent states

**Table 3.** Eigenstates of the NW in the strong Zeeman regime ( $E_Z > 4E_{SO}$ ). The meaning of symbols is the same as in table 1.

Strong Zeeman regime ( $E_Z > 4E_{SO}$ )			
Energy range	Propagating modes	Velocity	Evanescent modes
$-E_{SO} \left(1 + \frac{E_Z^2}{4E_{SO}^2}\right) < E < -\frac{E_Z^2}{4E_{SO}}$	No propagating mode		$\xi_1(\pm\kappa_-(E))e^{\pm\kappa_-(E)x}$ $\xi_1(\pm\kappa_+(E))e^{\pm\kappa_+(E)x}$ [ $\kappa_{\pm}(E) \in E_1$ band]
$-\frac{E_Z^2}{4E_{SO}} < E < -E_Z$	No propagating states		$\xi_1(\pm\kappa_-(E))e^{\pm\kappa_-(E)x}$ $\xi_2(\pm\kappa_+(E))e^{\pm\kappa_+(E)x}$ [ $\kappa_-(E) \in E_1$ band] [ $\kappa_+(E) \in E_2$ band]
$-E_Z < E < E_Z$	2 propagating states $\chi_1(\pm k_+(E))e^{\pm ik_+(E)x}$ [ $k_+(E) \in E_1$ band]	$\pm v_+(E)$	$\xi_2(\pm\kappa_+(E))e^{\pm\kappa_+(E)x}$ [ $\kappa_+(E) \in E_2$ band]
$E > E_Z$	4 propagating states $\chi_2(\pm k_-(E))e^{\pm ik_-(E)x}$ $\chi_1(\pm k_+(E))e^{\pm ik_+(E)x}$ [ $k_-(E) \in E_2$ band] [ $k_+(E) \in E_1$ band]	$\pm v_-(E)$ $\pm v_+(E)$	No evanescent states

## Appendix B. Details about the evaluation of the scattering matrix and the transmission coefficient

Here we provide the technical details concerning the determination of the transmission coefficient for the system with inhomogeneous RSOC setup, whence the conductance is straightforwardly determined from equation (10). To this purpose, one first has compute the transfer matrix. We exploit the fact that, since the system is mesoscopic, energy is conserved, and we can write the general solution as a superposition over the energy  $E$  of stationary solutions  $\hat{\Psi}_E(x, t) = \hat{\Psi}_E(x) e^{-iEt/\hbar}$ . In turn, in the  $j$ th region ( $j = L, R = 0, 1$ ) the field  $\hat{\Psi}_E(x)$  is expressed as a superposition of all possible modes (propagating and evanescent) characterizing the region at a fixed energy  $E$ . These modes can be selected from tables 1–3, depending on the parameter regime (Rashba-dominated, weakly or strongly Zeeman dominated) and the energy sub-range.

*The single interface case.* As an example, let us consider the case of one single interface at  $x = 0$ , and assume that the left side is in the Rashba-dominated regime, while the right side is in the strongly Zeeman-dominated regime. Moreover, let us consider an energy value inside the magnetic gap,  $|E| < E_Z$ .

As can be seen from tables 1 and 3, in this energy range there are two propagating modes and two evanescent modes on each side of the interface. Then, a scattering state has the form

$$\hat{\Psi}_E(x) = \frac{1}{\sqrt{2\pi\hbar}} \begin{cases} \frac{1}{\sqrt{v_+(E; \alpha_L)}} \left( \hat{a}_{1E}^{(L)} \chi_1(k_+(E; \alpha_L)) e^{ik_+(E; \alpha_L)x} + \hat{b}_{1E}^{(L)} \chi_1(-k_+(E; \alpha_L)) e^{-ik_+(E; \alpha_L)x} \right) & x < 0 \\ \quad + \hat{f}_{\beta_E E}^{(L)} \xi_{\beta_E}(\kappa_+(E; \alpha_L)) e^{\kappa_+(E; \alpha_L)x} & \\ \frac{1}{\sqrt{v_+(E; \alpha_R)}} \left( \hat{b}_{1E}^{(R)} \chi_1(k_+(E; \alpha_R)) e^{ik_+(E; \alpha_R)x} + \hat{a}_{1E}^{(R)} \chi_1(-k_+(E; \alpha_R)) e^{-ik_+(E; \alpha_R)x} \right) & x > 0 \\ \quad + \hat{g}_{2E}^{(R)} \xi_2(-\kappa_+(E; \alpha_R)) e^{-\kappa_+(E; \alpha_R)x} & \end{cases} \quad (\text{B1})$$

where  $\hat{a}_{1E}^{(L/R)}$  denotes the fermionic operator related to the propagating mode incoming from the left/right side (originating from the lower band  $\beta = 1$ ),  $\hat{b}_{1E}^{(L/R)}$  describes the one related to the propagating mode outgoing to the left/right (also originating from the lower band  $\beta = 1$ ), with  $\chi_1$  being the related spinor given in equation (A3). Similarly  $\hat{f}_{\beta_E E}^{(L)}$  and  $\hat{g}_{2E}^{(R)}$  are the evanescent mode operators and  $\xi_1, \xi_2$  denote the related spinors given in equations (A8) and (A9). For the Rashba-dominated side on the left, from table 1 one sees that the evanescent mode originates from the lower complex band ( $\beta_E = 1$ ) for  $E < -E_Z^2/4E_{SO}$  and from the upper complex band ( $\beta_E = 2$ ) for  $E > -E_Z^2/4E_{SO}$ , whereas for the strongly Zeeman-dominated side on the right we deduce from table 3 that the evanescent mode originates from the upper complex band ( $\beta = 2$ ) on the Zeeman-side. Inserting equation (B1) into the boundary conditions (9) at the interface  $x = 0$ , the latter can be rewritten in a matrix form as

$$M_E^{(L)}(0) \begin{pmatrix} \hat{a}_{1E}^{(L)} \\ \hat{b}_{1E}^{(L)} \\ \hat{f}_{\beta_E E}^{(L)} \\ 0 \end{pmatrix} = M_E^{(R)}(0) \begin{pmatrix} \hat{b}_{1E}^{(R)} \\ \hat{a}_{1E}^{(R)} \\ 0 \\ \hat{g}_{2E}^{(R)} \end{pmatrix} \quad (\text{B2})$$

where  $M_E^{(L/R)}(0) \in \mathbb{C}^{4 \times 4}$  are two  $4 \times 4$  complex boundary matrices at energy  $E$  given by

$$M_E^{(L)}(0) = \begin{pmatrix} \frac{\chi_1(k_+)}{\sqrt{v_+}} & \frac{\chi_1(-k_+)}{\sqrt{v_+}} & \xi_2(\kappa_+) & \xi_2(-\kappa_+) \\ i \frac{(k_+ - \sigma_L k_{SO,L}) \chi_1(k_+)}{\sqrt{v_+}} & -i \frac{(k_+ + \sigma_L k_{SO,L}) \chi_1(-k_+)}{\sqrt{v_+}} & (\kappa_+ - i\sigma_L k_{SO,L}) \xi_2(\kappa_+) & -(\kappa_+ + i\sigma_L k_{SO,L}) \xi_2(-\kappa_+) \end{pmatrix} \quad (\text{B3})$$

and

$$M_E^{(R)}(0) = \begin{pmatrix} \frac{\chi_1(k_+)}{\sqrt{v_+}} & \frac{\chi_1(-k_+)}{\sqrt{v_+}} & \xi_{\beta_E}(\kappa_+) & \xi_{\beta_E}(-\kappa_+) \\ i \frac{(k_+ - \sigma_R k_{SO,R}) \chi_1(k_+)}{\sqrt{v_+}} & -i \frac{(k_+ + \sigma_R k_{SO,R}) \chi_1(-k_+)}{\sqrt{v_+}} & (\kappa_+ - i\sigma_R k_{SO,R}) \xi_{\beta_E}(\kappa_+) & -(\kappa_+ + i\sigma_R k_{SO,R}) \xi_{\beta_E}(-\kappa_+) \end{pmatrix} \quad (\text{B4})$$

where  $\chi_1, \xi_1$  and  $\xi_2$  are the  $2 \times 1$  spinors in equations (A3), (A8) and (A9), respectively, and the dependence of  $\kappa_+$  and  $v_+$  on  $\alpha_L$  and  $E$  [in equation (B3)] and on  $\alpha_R$  and  $E$  [in equation (B4)] has been omitted for simplicity. Moreover, we have denoted  $\sigma_{R,L} = \text{sgn}(\alpha_{R,L})$  and we have used the fact that the second equation (9) at the interface  $x = 0$  can be rewritten as

$$\partial_x \hat{\Psi}(0^-) = \partial_x \hat{\Psi}(0^+) - i(\sigma_R k_{SO,R} - \sigma_L k_{SO,L}) \sigma_z \hat{\Psi}(0) \quad (\text{B5})$$

in terms of the spin-orbit wavevectors (14). From equation (B2), the transfer matrix relating the operators on the right side of interface to the operators on the left side,

$$\begin{pmatrix} \hat{b}_{1E}^{(R)} \\ \hat{a}_{1E}^{(R)} \\ 0 \\ \hat{g}_{2E}^{(R)} \end{pmatrix} = W_E \begin{pmatrix} \hat{a}_{1E}^{(L)} \\ \hat{b}_{1E}^{(L)} \\ \hat{f}_{\beta_E E}^{(L)} \\ 0 \end{pmatrix}, \quad |E| < E_Z \quad (\text{B6})$$

is straightforwardly found to be  $W_E = [M_E^{(R)}(0)]^{-1} M_E^{(L)}(0)$ . Since equation (B6) represent four constraints for the six unknown operators, one can express four of them in terms of the incoming operators  $\hat{a}_{1E}^{(L)}$  and  $\hat{a}_{1E}^{(R)}$ . In particular, one can thus compute the scattering matrix  $S_E$ , which relates the outgoing propagating

modes to the incoming ones

$$\begin{pmatrix} \hat{b}_{1E}^{(L)} \\ \hat{b}_{1E}^{(R)} \end{pmatrix} = \underbrace{\begin{pmatrix} r_E & t'_E \\ t_E & r'_E \end{pmatrix}}_{S_E} \begin{pmatrix} \hat{a}_{1E}^{(L)} \\ \hat{a}_{1E}^{(R)} \end{pmatrix} \quad (B7)$$

The transmission coefficient is computed as  $T(E) = |t_E|^2 = |t'_E|^2$  and the linear conductance in the considered range  $|E_F| < E_Z$  is obtained from equation (10).

In a similar way, one can find the transmission in the energy range  $E > E_Z$  above the gap. In such a case, on each side of the interface there are two propagating modes and no evanescent mode on each side, so that the scattering state solution now acquires the form

$$\hat{\Psi}_E(x) = \frac{1}{\sqrt{2\pi\hbar}} \begin{cases} \frac{1}{\sqrt{v_+(E; \alpha_L)}} \left( \hat{a}_{1E}^{(L)} \chi_1(k_+(E; \alpha_L)) e^{ik_+(E; \alpha_L)x} + \hat{b}_{1E}^{(L)} \chi_1(-k_+(E; \alpha_L)) e^{-ik_+(E; \alpha_L)x} \right) \\ + \frac{1}{\sqrt{v_-(E; \alpha_L)}} \left( \hat{a}_{2E}^{(L)} \chi_2(k_-(E; \alpha_L)) e^{ik_-(E; \alpha_L)x} + \hat{b}_{2E}^{(L)} \chi_2(-k_-(E; \alpha_L)) e^{-ik_-(E; \alpha_L)x} \right) & x < 0 \\ \frac{1}{\sqrt{v_+(E; \alpha_R)}} \left( \hat{b}_{1E}^{(R)} \chi_1(k_+(E; \alpha_R)) e^{ik_+(E; \alpha_R)x} + \hat{a}_{1E}^{(R)} \chi_1(-k_+(E; \alpha_R)) e^{-ik_+(E; \alpha_R)x} \right) \\ + \frac{1}{\sqrt{v_-(E; \alpha_R)}} \left( \hat{b}_{2E}^{(R)} \chi_2(k_-(E; \alpha_R)) e^{ik_-(E; \alpha_R)x} + \hat{a}_{2E}^{(R)} \chi_2(-k_-(E; \alpha_R)) e^{-ik_-(E; \alpha_R)x} \right) & x > 0 \end{cases} \quad (B8)$$

Inserting equation (B8) into the boundary conditions (9) and proceeding as outlined above, one can find the transfer matrix

$$\begin{pmatrix} \hat{a}_{1E}^{(R)} \\ \hat{b}_{1E}^{(R)} \\ \hat{a}_{2E}^{(R)} \\ \hat{b}_{2E}^{(R)} \end{pmatrix} = W_E \begin{pmatrix} \hat{a}_{1E}^{(L)} \\ \hat{b}_{1E}^{(L)} \\ \hat{a}_{2E}^{(L)} \\ \hat{b}_{2E}^{(L)} \end{pmatrix} \quad (B9)$$

whence the scattering matrix  $S_E$ , which is now a  $4 \times 4$  matrix, can straightforwardly be obtained

$$\begin{pmatrix} \hat{b}_{1E}^{(L)} \\ \hat{b}_{2E}^{(L)} \\ \hat{b}_{1E}^{(R)} \\ \hat{b}_{2E}^{(R)} \end{pmatrix} = \underbrace{\begin{pmatrix} r_E & t'_E \\ t_E & r'_E \end{pmatrix}}_{S_E} \begin{pmatrix} \hat{a}_{1E}^{(L)} \\ \hat{a}_{2E}^{(L)} \\ \hat{a}_{1E}^{(R)} \\ \hat{a}_{2E}^{(R)} \end{pmatrix} \quad (B10)$$

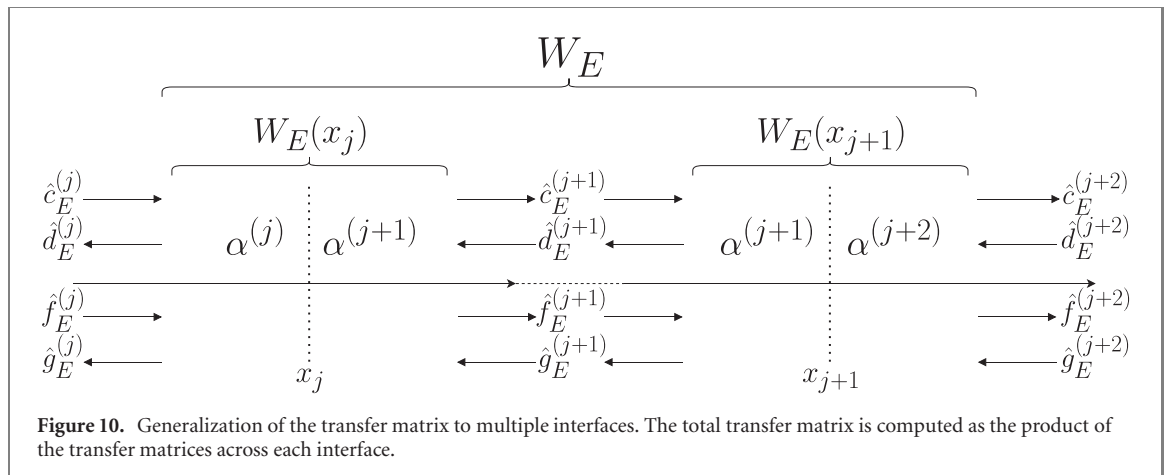
with  $\mathbf{t}, \mathbf{t}'$  and  $\mathbf{r}, \mathbf{r}'$  denoting the  $2 \times 2$  transmission and reflection blocks. The transmission coefficient is now obtained as  $T(E) = \text{tr}[\mathbf{t}_E^\dagger \mathbf{t}_E] = \text{tr}[\mathbf{t}'_E \mathbf{t}'_E^\dagger]$ .

*Generalization to multiple interfaces.* It is straightforward to generalise the same approach to the case of  $N$  interfaces. Let us consider an interface located at  $x_j$  separating a region with RSOC  $\alpha_j$  (on the left side) from a region with RSOC  $\alpha_{j+1}$  on the right, as depicted in figure 10. Similarly to the single interface problem [see equations (B1) and (B8)], on each side of the interface the electron field operator  $\hat{\Psi}_E(x)$  is written as an expansion of (at most) four modes, which can be propagating or evanescent, depending on the specific regime of that region and on the energy range, according to tables 1–3. Denoting by  $\hat{c}_E^{(j)}, \hat{d}_E^{(j)}, \hat{f}_E^{(j)}$ , and  $\hat{g}_E^{(j)}$  the operators related to the above four modes on the  $j$ th region and the boundary conditions (9) can be rewritten in a matrix form

$$M_E^{(j)}(x_j) \begin{pmatrix} \hat{c}_E^{(j)} \\ \hat{d}_E^{(j)} \\ \hat{f}_E^{(j)} \\ \hat{g}_E^{(j)} \end{pmatrix} = M_E^{(j+1)}(x_j) \begin{pmatrix} \hat{c}_E^{(j+1)} \\ \hat{d}_E^{(j+1)} \\ \hat{f}_E^{(j+1)} \\ \hat{g}_E^{(j+1)} \end{pmatrix} \quad (B11)$$

The transfer matrix across the interface at  $x_j$  is obtained as  $W_E(x_j) = [M_E^{(j+1)}(x_j)]^{-1} M_E^{(j)}(x_j)$ . Then, by observing that the operators on right of the interface  $x_j$  are the very same operators as the ones on the left of the interface at  $x_{j+1}$  (see figure 10), the total transfer matrix  $W_E$  across the entire inhomogeneous scattering region

$$\begin{pmatrix} \hat{c}_E^{(N)} \\ \hat{d}_E^{(N)} \\ \hat{f}_E^{(N)} \\ \hat{g}_E^{(N+1)} \end{pmatrix} = W_E \begin{pmatrix} \hat{c}_E^{(0)} \\ \hat{d}_E^{(0)} \\ \hat{f}_E^{(0)} \\ \hat{g}_E^{(0)} \end{pmatrix} \quad (B12)$$



can be easily found as the product  $W_E = \prod_{j=0}^{N-1} W_E(x_{N-j-1})$ . For instance, for the doubly gated NW problem of section 5, the total transfer matrix is the product  $W_E = W_E(x_1)W_E(x_0)$  of the two single-interface transfer matrices and contains the distance  $d = x_1 - x_0$  between the two interfaces at  $x_0$  and  $x_1$ . Finally, one observes that in the outer region  $j = 0$  (left lead) the modes propagating rightwards (leftwards) are incoming to (outgoing from) the scattering region and can thus be relabelled as  $\hat{a}_{\beta E}^{(L)}$  ( $\hat{b}_{\beta E}^{(L)}$ ). Moreover, in order to ensure the normalizability of the state, only the evanescent mode decaying to the left is admitted, like in equation (B1). Effectively, this means that in equation (B11), the operator related to the mode diverging on the left has to be set to zero, like in equation (B6). Similarly, in the outer region  $j = N$  (right lead) the modes propagating leftwards (rightwards) are incoming (outgoing) and are relabelled as  $\hat{a}_{\beta E}^{(R)}$  ( $\hat{b}_{\beta E}^{(R)}$ ), while only the evanescent mode decaying on the right, if any, is admitted. Implementing these aspects in equation (B11), and re-expressing the outgoing mode operators  $\hat{b}_{\beta E}^{(L)}$ ,  $\hat{b}_{\beta E}^{(R)}$  in terms of the incoming ones  $\hat{a}_{\beta E}^{(L)}$ ,  $\hat{a}_{\beta E}^{(R)}$ , one finds the scattering matrix similarly to what was done in equations (B7) and (B10) for the single interface case.

## ORCID iDs

Leonid Gogin  <https://orcid.org/0000-0001-7248-3740>

Fausto Rossi  <https://orcid.org/0000-0001-6729-0928>

Fabrizio Dolcini  <https://orcid.org/0000-0001-9550-9106>

## References

- [1] Lutchyn R M, Sau J D and Das Sarma S 2010 *Phys. Rev. Lett.* **105** 077001
- [2] Oreg Y, Refael G and von Oppen F 2010 *Phys. Rev. Lett.* **105** 177002
- [3] Alicea J 2012 *Rep. Prog. Phys.* **75** 076501
- [4] Aguado R 2017 *La Rivista del Nuovo Cimento* **40** 523
- [5] Prada E et al 2020 *Nat. Rev. Phys.* **2** 575
- [6] Val'kov V V, Shustin M S, Aksenov S V, Zlotnikov A O, Fedoseev A D, Mitskan V A and Kagan M Y 2022 *Phys. Usp.* **65** 2
- [7] Mourik V, Zuo K, Frolov S M, Plissard S R, Bakkers E P A M and Kouwenhoven L P 2012 *Science* **336** 1003
- [8] Rokhinson L P, Liu X and Furdyna J K 2012 *Nat. Phys.* **8** 795
- [9] Das A, Ronen Y, Most Y, Oreg Y, Heiblum M and Shtrikman H 2012 *Nat. Phys.* **8** 887
- [10] Deng M T, Yu C L, Huang G Y, Larsson M, Caroff P and Xu H Q 2012 *Nano Lett.* **12** 6414
- [11] Lee E J H, Jiang X, Houzet M, Aguado R, Lieber C M and De Franceschi S 2014 *Nat. Nanotechnol.* **9** 79
- [12] Albrecht S M, Higginbotham A P, Madsen M, Kuemmeth F, Jespersen T S, Nygård J, Krogstrup P and Marcus C M 2016 *Nature* **531** 206
- [13] Deng M T, Vaitiekėnas S, Hansen E B, Danon J, Leijnse M, Flensberg K, Nygård J, Krogstrup P and Marcus C M 2016 *Science* **354** 1557
- [14] Gül Ö et al 2018 *Nat. Nanotechnol.* **13** 192
- [15] Kallaher R L, Heremans J J, Goel N, Chung S J and Santos M B 2010 *Phys. Rev. B* **81** 035335
- [16] van Weperen I, Plissard S R, Bakkers E P A M, Frolov S M and Kouwenhoven L P 2013 *Nano Lett.* **13** 387
- [17] Kammhuber J et al 2016 *Nano Lett.* **16** 3482
- [18] Heedt S, Prost W, Schubert J, Grützmacher D and Schäpers T 2016 *Nano Lett.* **16** 3116
- [19] Li S, Kang N, Fan D X, Wang L B, Huang Y Q, Caroff P and Xu H Q 2016 *Sci. Rep.* **6** 24822
- [20] Zhang H et al 2017 *Nat. Commun.* **8** 16025
- [21] Fadaly E M T et al 2017 *Nano Lett.* **17** 6511
- [22] Estrada Saldaña J C, Niquet Y-M, Cleuziou J-P, Lee E J H, Car D, Plissard S R, Bakkers E P A M and De Franceschi S 2018 *Nano Lett.* **18** 2282

- [23] Aseev P et al 2019 *Nano Lett.* **19** 9102
- [24] Badawy G, Gazibegovic S, Borsoi F, Heedt S, Wang C A, Koelling S, Verheijen M A, Kouwenhoven L P and Bakkers E P A M 2019 *Nano Lett.* **19** 3575
- [25] Zellekens P et al 2020 *Semicond. Sci. Technol.* **35** 085003
- [26] Iorio A, Rocci M, Bours L, Carrega M, Zannier V, Sorba L, Roddaro S, Giazotto F and Strambini E 2019 *Nano Lett.* **19** 652
- [27] Plissard S R et al 2012 *Nano Lett.* **12** 1794
- [28] Singh A P, Roccapriore K, Algarni Z, Salloom R, Golden T D and Philipose U 2019 *Nanomaterials* **9** 1260
- [29] Liu Y et al 2020 *Nano Lett.* **20** 456
- [30] Sasaki S, Tateno K, Zhang G, Suominen H, Harada Y, Saito S, Fujiwara A, Sogawa T and Muraki K 2013 *Appl. Phys. Lett.* **103** 213502
- [31] Burke A M, Carrad D J, Gluschke J G, Storm K, Fahlvik Svensson S, Linke H, Samuelson L and Micolich A P 2015 *Nano Lett.* **15** 2836
- [32] Takase K, Ashikawa Y, Zhang G, Tateno K and Sasaki S 2017 *Sci. Rep.* **7** 930
- [33] Das S R 2019 *Nanoelectronics: Devices, Circuits and Systems* ed B K Kaushik (Amsterdam: Elsevier) p 355 ch 11
- [34] Yin Y, Zhang Z, Zhong H, Shao C, Wan X, Zhang C, Robertson J and Guo Y 2021 *ACS Appl. Mater. Interfaces* **13** 3387
- [35] Takase K, Tateno K and Sasaki S 2021 *Appl. Phys. Lett.* **119** 013102
- [36] Liang D and Gao X P A 2012 *Nano Lett.* **12** 3263
- [37] Slomski B, Landolt G, Muff S, Meier F, Osterwalder J and Hugo Dil J H 2013 *New J. Phys.* **15** 125031
- [38] van Weperen I, Tarasinski B, Eeltink D, Pribiag V S, Plissard S R, Bakkers E P A M, Kouwenhoven L P and Wimmer M 2015 *Phys. Rev. B* **91** 201413
- [39] Bercioux D and Lucignano P 2015 *Rep. Prog. Phys.* **78** 106001
- [40] Scherübl Z, Fülöp G, Madsen M H, Nygård J and Csonka S 2016 *Phys. Rev. B* **94** 035444
- [41] Bindel J R, Pezzotta M, Ulrich J, Liebmann M, Sherman E Y and Morgenstern M 2016 *Nat. Phys.* **12** 920
- [42] Borge J and Tokatly I V 2017 *Phys. Rev. B* **96** 115445
- [43] Kloeffel C, Rančić M J and Loss D 2018 *Phys. Rev. B* **97** 235422
- [44] Wójcik P, Bertoni A and Goldoni G 2018 *Phys. Rev. B* **97** 165401
- [45] Premasiri K and Gao X P A 2019 *J. Phys.: Condens. Matter* **31** 193001
- [46] Shcherbakov D et al 2021 *Sci. Adv.* **7** eabe2892
- [47] Nagasawa F, Reynoso A A, Baltanás J P, Frustaglia D, Saarikoski H and Nitta J 2018 *Phys. Rev. B* **98** 245301
- [48] Krupin O, Bihlmayer G, Starke K, Gorovikov S, Prieto J E, Döbrich K, Blügel S and Kaindl G 2005 *Phys. Rev. B* **71** 201403
- [49] Slomski B, Landolt G, Muff S, Meier F, Osterwalder J and Hugo Dil J H 2013 *New J. Phys.* **15** 125031
- [50] Tsai H, Karube S, Kondou K, Yamaguchi N, Ishii Y and Otani Y 2018 *Sci. Rep.* **8** 5564
- [51] Wang W, Li X M and Fu J Y 2016 *J. Magn. Magn. Mater.* **411** 84
- [52] Malard M, Grusha I, Japaridze G I and Johannesson H 2011 *Phys. Rev. B* **84** 075466
- [53] Strěda P and Šeba P 2003 *Phys. Rev. Lett.* **90** 256601
- [54] Quay C H L, Hughes T L, Sulpizio J A, Pfeiffer L N, Baldwin K W, West K W, Goldhaber-Gordon D and de Picciotto R 2010 *Nat. Phys.* **6** 336
- [55] Kloeffel C, Trif M and Loss D 2011 *Phys. Rev. B* **84** 195314
- [56] Cheng M and Lutchyn R M 2012 *Phys. Rev. B* **86** 134522
- [57] Szumniak P, Chevallier D, Loss D and Klinovaja J 2017 *Phys. Rev. B* **96** 041401
- [58] Klinovaja J and Loss D 2015 *Eur. Phys. J. B* **88** 62
- [59] Rossi L, Dolcini F and Rossi F 2020 *Eur. Phys. J. Plus* **135** 597
- [60] Rossi L, Dolcini F and Rossi F 2020 *Phys. Rev. B* **101** 195421
- [61] Glazov M M and Sherman E Y 2007 *Phys. Rev. Lett.* **107** 156602
- [62] Tserkovnyak Y, Halperin B I, Kovalev A A and Brataas A 2007 *Phys. Rev. B* **76** 085319
- [63] Sadreev A F and Sherman E Y 2013 *Phys. Rev. B* **88** 115302
- [64] Kudła S, Dyrdał A, Dugaev V K, Sherman E Y and Barnaś J 2018 *Phys. Rev. B* **97** 245307
- [65] Rashba E I 2004 *Phys. Rev. B* **70** 161201
- [66] Dolcini F and Rossi F 2018 *Phys. Rev. B* **98** 045436
- [67] Sánchez D and Serra L 2006 *Phys. Rev. B* **74** 153313
- [68] Note that the boundary conditions (9), when rewritten in terms of  $\hat{\Psi}'$  through equation (3), acquire the standard form of continuity of the spinor field  $\hat{\Psi}'$  and its derivative  $\partial_x \hat{\Psi}'$ .
- [69] Datta S 1995 *Electronic Transport in Mesoscopic Systems* (Cambridge: Cambridge University Press)
- [70] Sánchez D, Serra L and Choi M-S 2008 *Phys. Rev. B* **77** 035315
- [71] Cayao J, Prada E, San-Jose P and Aguado R 2015 *Phys. Rev. B* **91** 024514
- [72] Rainis D and Loss D 2014 *Phys. Rev. B* **90** 235415
- [73] Although the two configurations (Zeeman, Rashba) and (Rashba, Zeeman) with exchanged values, are *a priori* physically different because of the magnetic field applied along the NW axis, they actually yield the same transmission coefficient  $T(E)$ , for the latter turns out to be independent of the sign of the magnetic field along the NW. This can be seen by performing the gauge transformation  $\hat{\Psi} \rightarrow \hat{\Psi}' = \sigma_z \hat{\Psi}$  on the electron field in the Hamiltonian equation (1), which maps the case of Zeeman field  $+h_{\perp}$  into the case  $-h_{\perp}$ .
- [74] Bound states localized at the interface may exist, but they are energetically located below the continuum, not in the magnetic gap range (see reference [60]).
- [75] Gogin L, Rossi L, Rossi F and Dolcini F 2022 *New J. Phys.* **24** 053045
- [76] Takase K, Zhang G, Tateno K and Sasaki S 2019 *NTT Tech. Rev.* **17** 56
- [77] Peres N M R 2009 *J. Phys.: Condens. Matter* **21** 095501
- [78] Mal'shukov A G, Tang C S, Chu C S and Chao K A 2003 *Phys. Rev. B* **68** 233307
- [79] Tang C S, Mal'shukov A G and Chao K A 2005 *Phys. Rev. B* **71** 195314
- [80] Dolcini F 2012 *Phys. Rev. B* **85** 033306
- [81] Klinovaja J, Stano P and Loss D 2016 *Phys. Rev. Lett.* **116** 176401